



저작자표시-비영리-변경금지 2.0 대한민국

이용자는 아래의 조건을 따르는 경우에 한하여 자유롭게

- 이 저작물을 복제, 배포, 전송, 전시, 공연 및 방송할 수 있습니다.

다음과 같은 조건을 따라야 합니다:



저작자표시. 귀하는 원저작자를 표시하여야 합니다.



비영리. 귀하는 이 저작물을 영리 목적으로 이용할 수 없습니다.



변경금지. 귀하는 이 저작물을 개작, 변형 또는 가공할 수 없습니다.

- 귀하는, 이 저작물의 재이용이나 배포의 경우, 이 저작물에 적용된 이용허락조건을 명확하게 나타내어야 합니다.
- 저작권자로부터 별도의 허가를 받으면 이러한 조건들은 적용되지 않습니다.

저작권법에 따른 이용자의 권리는 위의 내용에 의하여 영향을 받지 않습니다.

이것은 [이용허락규약\(Legal Code\)](#)을 이해하기 쉽게 요약한 것입니다.

[Disclaimer](#)

공학박사학위논문

터보펌프 인듀서의 날개 수와 현절비가
성능 및 캐비테이션 불안정성에 미치는
영향

Effects of the Blade Number and Solidity on the
Performance and Cavitation Instabilities of a
Turbopump Inducer

2015년 8월

서울대학교 대학원

기계항공공학부

강 병 윤

터보펌프 인듀서의 날개 수와 현절비가
성능 및 캐비테이션 불안정성에 미치는
영향

Effects of the Blade Number and Solidity on the
Performance and Cavitation Instabilities of a
Turbopump Inducer

지도교수 송 성 진

이 논문을 공학박사 학위논문으로 제출함

2015년 6월

서울대학교 대학원

기계항공공학부

강 병 윤

강병윤의 공학박사 학위논문을 인준함

2015년 6월

위 원 장 : _____

부위원장 : _____

위 원 : _____

위 원 : _____

위 원 : _____

Effects of the Blade Number and Solidity on the Performance and Cavitation Instabilities of a Turbopump Inducer

Seoul National University
School of Mechanical and Aerospace Engineering
Byung Yun Kang

Abstract

The turbopump used in a liquid rocket propulsion system generates cavitation at the inlet because of the high rotating speed. To improve the suction performance, an inducer was installed at the front impeller. Cavitation instabilities, such as cavitation surge, rotating cavitation, and asymmetric cavitation, occur on the shaft vibration and noise. These phenomena can lead to the destruction of the impeller. Therefore, the proper suction performance and instabilities control are required when an inducer designing. Recently, many studies have been reported in which an experiment test and numerical analysis for the turbopump inducer were performed. Researches confirmed the differences in the performance and the efficiency for shape modifications and scales. Studies have also been carried out on the blade angle, tip clearance, and solidity of design

parameters. The number of blade, which is one of the important parameters, has a very significant impact on the head, the suction performance, and instabilities of the turbopump. However, in the previous studies, the number of blade is simply changed with respect to the same axial length. In other words, as the number of the blade increases, the solidity also changes at the same time. Thus, as reported in these studies, this effect makes it difficult to determine whether the influence is due to the blade number or the solidity. For this reason, in this study, the performance, the efficiency, and cavitation instabilities were evaluated in which the different blade number for the inducers with the same solidity. To analyze the solidity effect, the different blade number for an inducer with respect to the same axial length was included together. Flow characteristics were evaluated using the numerical calculation, and the verification of the validity and the reliability of results were obtained by performing the experiment test

The total pressure rise of Z3s3 of the experiment test was 12.75 % smaller than that of Z2s2 at design mass flow rate, and the total pressure rise of Z3s2 decreased by 18.74 % less than that of Z2s2. The efficiency of Z2s2 was the highest and then, the values of Z3s2 and Z3s3 were followed.

The mass averaged deviation angle of Z3s2 was smaller than that of Z2s2 which represents comparison of the blade number effect. The mass averaged deviation angle of Z3s2 was larger than that of Z3s3. This trend was satisfied with the empirical rule.

The relative total pressure loss for all three cases increased while

passing the inducer. Especially, the losses of Z3s3 and Z3s2 were bigger than that of Z3s2, and continue to the impeller inlet. Those loss characteristics influenced on the efficiency. Therefore, the efficiency of Z3s3 was the lowest compared with other cases, even though the pressure rise performance of Z3s3 was higher than that of Z3s2.

The existing efficiency empirical equation did not reflect to the blade number. So the new empirical equation was suggested by applying the blade number effect. To get the reliability, two more models were added. The efficiencies of Z3s4 and Z4s2 were reflected the correction between the numerical calculation and the experiment test.

The suction performance curve of the inducer used for this study at design mass flow rate. The *NPSH_r* of Z3s3 and Z3s2 increased 25.8% and 14.1%, respectively. The biggest cause for the difference between the experiment test and the numerical calculation was the cavitation model. The empirical equation of *NPSH_r* was included with valuables of the blade number and the solidity. However, the result had a big difference.

As the inlet pressure decreased from non cavitation condition, cavitation occurred at blade tip that called the tip vortex cavitation. And then, the tip vortex cavitation was getting longer and connected to the bubble cavitation increasingly. Cavitation inception was not related to the solidity, and only depended on the blade number.

The pressure of the fluid coming to the leading edge reduced due to the interference with the next blade. Because of this phenomenon, the head drop started once the cavity occurred on the suction surface.

As the inlet pressure decreased, a symmetry cavitation corresponding to 2 or 3 times the rotational speed appeared. An asymmetry cavitation corresponding to the rotational speed also occurred. Cavitation surge occurred at low frequency when the inlet pressure decreases further. In case of the three bladed inducers, rotating cavitation was strongly observed. In case of the Z3s2, it was found that the intensity of symmetry cavitation and rotating cavitation significantly weak compared with case of the Z3s3. Especially, higher order rotating cavitation did not occur.

Keywords: Turbopump, Inducer, Empirical equation, Cavitation, *NPSH*, Instability, Cavitation inception

Student Number: 2008-22864

Contents

Abstract	i
Contents	v
List of Figures	vii
List of Tables	xi
Nomenclature	xii
Chapter 1. Introduction	1
1.1 Background	1
1.2 Inducer design	3
1.3 Problem description	6
1.4 Research objectives	8
Chapter 2. Research Method	14
2.1 Inducer model	14
2.2 Experimental analysis	14
2.3 Numerical analysis	16
2.4 Comparison with measured data	18

Chapter 3. Hydraulic Performance	32
3.1 Pressure rise	32
3.2 Work coefficient	33
3.3 Efficiency	34
3.4 Comparison of deviation angle and circumferential velocity	35
3.5 Comparison of head	37
3.6 Comparison of relative total pressure	38
Chapter 4. Empirical Equation	55
4.1 Deviation angle	55
4.2 Efficiency	57
Chapter 5. Cavitation Instability	68
5.1 Fundamental of cavitation	68
5.2 Various type of cavitation	70
5.3 Cavitation model	74
5.4 Required <i>NPSH</i>	79
5.5 Cavitation inception	82
5.6 Effects of blade number and solidity	84
Chapter 6. Conclusions	101
6.1 Conclusions	101
6.2 Recommendations for future work	103
References	105
Abstract (in Korean)	111

List of Figures

1.1	KSLV-I	9
1.2	Capability of 30,000 Kg Turbopump	10
1.3	Pressure equilibrium of the inducer design.....	10
1.4	Effect of the inducer on the cavitation performance	11
1.5	Velocity triangle of the inducer inlet	11
1.6	Velocity triangle of the inducer outlet	12
1.7	Static pressure coefficients with respect to the tip clearance	12
1.8	<i>NPSH_r</i> of the inducer	13
1.9	Head and efficiency performance	13
2.1	Inducer: (a) Z2s2; (b) Z3s3; (c) Z3s2	22
2.2	Effect of Reynolds number on the efficiency	23
2.3	Schematic of the test facility.	24
2.4	Test section of the inducer	24
2.5	Calibration: (a) for torque transducer; (b) for pressure transducer	25
2.6	Validation of the repeatability experiment test	26
2.7	Non dimensional pressure rise performance	26
2.8	Computational domain for a turbopump	27
2.9	Computational grid of an inducer	27
2.10	Grid dependency test: Comparison of the static pressure coefficient	28
2.11	Comparison of the turbulence model for the static pressure	

coefficient	28
2.12 Relative velocity distributions from hub to tip	29
2.13 Tangential velocity distributions from hub to tip	29
2.14 Axial velocity distributions from hub to tip	30
2.15 Location of the data measurement	31
2.16 Comparison the static pressure at inducer outlet	31
3.1 Pressure rise performance: (a) w/o correction; (b) w/ correction	40
3.2 (a) Torque; (b) Work coefficient	41
3.3 Efficiency performance	42
3.4 Data uncertainty for the efficiency	43
3.5 Location of the inducer outlet	43
3.6 Axial velocity distribution for Z2s2	44
3.7 Relative circumferential velocity distribution for Z2s2	44
3.8 Deviation angle distribution for Z2s2	45
3.9 Circumferential velocity distribution for Z2s2	45
3.10 Effect of the blade number on the deviation angle distribution at location A	46
3.11 Effect of the solidity on the deviation angle distribution at location A	46
3.12 Deviation angle distribution: (a) at location A; (b) at location B	47
3.13 Circumferential velocity distribution: (a) at location A; (b) at location B	48
3.14 Effect of the blade number on the head distribution	

	of the inducer	49
3.15	Effect of the solidity on the head distribution of the inducer	49
3.16	Head distribution of the inducer for the three cases	50
3.17	Static head distribution: (a) CFD; (b) EXP	51
3.18	Relative total pressure loss characteristic at mid span:	
	(a) Z2s2; (b) Z3s3; (c) Z3s2	52
3.19	Relative total pressure loss characteristic at 90 % span:	
	(a) Z2s2; (b) Z3s3; (c) Z3s2	53
3.20	Radial and tangential mass averaged relative total pressure loss coefficient at an inducer	54
3.21	Relative velocity distribution at an inducer outlet	54
4.1	Deviation angle distribution for an inducer	61
4.2	Comparison of the efficiency empirical equation with the experiment test	62
4.3	Inducer Models: (a) Z3s4 ; (b) Z4s2	63
4.4	Comparison of the pressure rise performance	63
4.5	Comparison of the efficiency empirical equation with the numerical calculation	64
4.6	Factor of the solidity	65
4.7	Factor of the blade number	66
4.8	Comparison of the new efficiency empirical equation with the experiment test	67
5.1	Phase diagram of the water	86
5.2	Type of the cavitation	86
5.3	Schematic of cavitation performance showing the three key	

	cavitation numbers	87
5.4	Suction performance in the experiment test at design mass flow rate($\phi = 0.101$).	88
5.5	Comparison of the suction performance	89
5.6	Visualization of the cavitation inception: (a) Z2s2; (b) Z3s3; (c) Z3s2	89
5.7	Static pressure distribution at leading edge	90
5.8	Comparison of the cavitation inception	90
5.9	Head drop point for the numerical calculation	91
5.10	Static pressure recovery coefficient: (a) Z3s3; (b) Z3s2	92
5.11	Shape of the cavity: (a) Z3s3; (b) Z3s2	93
5.12	Visualization of cavitation in Z2s2	94
5.13	Visualization of cavitation in Z3s3	95
5.14	Visualization of cavitation in Z3s2	96
5.15	Schematic of the inducer blade: (a) w/o camber; (b) w/ camber (c) blade angel	97
5.16	Blade shape of the inducer	98
5.17	Comparison of the blade angle	98
5.18	FFT analysis of cavitation instabilities: (a) Z2s2; (b) Z3s3; (c) Z3s2	99

List of Tables

2.1	Specification of the inducers	23
4.1	Deviation angle of inducers	61
5.1	Required <i>NPSH</i> and the critical cavitation number	88

Nomenclatures

Roman Symbols

A	Inducer area
C	Absolute velocity
C_p	Static pressure recovery coefficient = $\frac{p - P_{in}}{\frac{1}{2}\rho U_t^2}$
CF	Correction factor
D	Diameter
f	Frequency
g	Gravitational acceleration
H	Head
i	Incidence = $\beta_1 - \beta_{1b}$
K	Relative total pressure loss coefficient = $\frac{P_{trel\ in} - P_{trel}}{\frac{1}{2}\rho U_t^2}$
l	Blade length
\dot{m}	Mass flow rate
$NPSH$	Net positive suction head = $\frac{P_t - P_v}{\rho g}$
p	Static pressure
P_t	Total pressure
Q	Flow rate

R	Radius
s	Solidity
t	Thickness of blade
U_t	Tip speed of inducer
W	Relative velocity
w	Angular velocity
Z	Blade number
α	Absolute flow angle
β	Relative flow angle
γ	Wedge angle
δ	Deviation angle
ρ	Density
λ	Blade cavitation coefficient
σ	Cavitation number = $\frac{P_t - P_v}{\frac{1}{2}\rho U_t^2}$
ϕ	Flow coefficient = Q/AU_t
η	Efficiency = $\eta = \frac{\rho g H Q}{T w} = \frac{g H}{U_2 C_{\theta 2}}$
ψ	Pressure rise coefficient = $g H / U_t^2$

Subscripts

1	Inducer inlet
2	Inducer exit

<i>b</i>	Blade angle
<i>corr</i>	Correction
<i>m</i>	Meridional value
<i>rel</i>	Relative value
<i>h</i>	Hub value
<i>in</i>	Inlet value
<i>p</i>	Pump value
<i>t</i>	Total value
<i>v</i>	Vapor value
<i>x</i>	Axial value
θ	Tangential value

Superscripts

*	Nominal value
---	---------------

Acronyms

BPF	Blade passing frequency
CFD	Computational fluid dynamics (Numerical calculated data)
EXP	Experimentally measured data
FFT	Fast Fourier transform

Chapter 1. Introduction

1.1 Background

In a liquid-rocket-propulsion system, a turbopump-feed cycle to produce high pressure fluid for feeding a combustion chamber is preferred to a pressure-feed cycle because of the relatively lower system weight and the better performance. Fig 1.1 shows the KSLV-I that KARI and Russia cooperated in developing the first Korean space launch vehicle. This launch vehicle is also used by a turbopump system. a liquid rocket propulsion system usually used two turbopumps. One is the oxidizer pump and another is the propellant pump. Both are driven by one shaft as shown in Fig 1.2.

Most turbopumps are centrifugal types: the fluid enters the pump near the rotating axis and the impeller accelerated the working fluid to high speed. The fluid flows radially outward into a diffuser and a volute which turns the high kinetic energy into high pressure energy. Compared to the axial turbopump, centrifugal pumps tend to permit much higher pressure. However, axial turbopumps still useful because it is commonly used as an inducer just upstream of the inlet of the impeller, which cause a rise in the inlet pressure to prevent substantial performance loss and strong unsteady forces acting on the pump component due to cavitation phenomena.

The inducer is the axial inlet portion of the turbopump rotor whose function is to raise the inlet head by an amount sufficient to preclude cavitation in the following stage. The inducer may be an integral part of the turbopump rotor or it may be mounted separately on the turbopump shaft upstream of the impeller. The principal objective in the design of an inducer is the attainment of high suction performance, but the achievement of maximum performance is limited by structural design considerations. Such a design depends on simultaneous satisfactory solutions of hydrodynamic and mechanical problems. An inducer is usually composed of quite thin impellers with high solidity (ratio of blade chord to spacing) and has 2, 3 or 4 blade. Cavitation usually forms in the early portion of the passage and collapse before reaching the main pump. It is designed to operate at small incidence angles with thin blade so that the perturbation to the flow and the resulting production of cavitation can be minimized. If one designs the inducer to function at a zero incidence angle at design mass flow rate, through even small flow perturbation, it can form cavitation on either the pressure or suction surfaces and can cause the cavitation oscillation between the two. To eliminate this uncertainty and ensure suction surface cavitation, inducers operating at an incidence angle of a few degrees are preferable.

Although the inducer is a simple helical-shaped axial pump, internal flow fields are characterized by complex properties: three-dimensional, unsteady, turbulent, almost incompressible in single phase flow and highly compressible in two-phase flow. Recently, since installing an inducer stage is common in rocket engine turbopumps, there are many

authors who have studied the flow in the inducer of pump under non-cavitation or cavitation conditions numerically and experimentally.

1.2 Inducer design

In general, an inducer provides a impeller to a high pressure fluid without the suction performance decrease when an inlet pressure is lower than the vapor pressure. Fig 1.3 and Fig. 1.4 show the basic concept of the inducer design. it is greatly to consider the following when an inducer is designed:

- (1) Calculate the inducer head to eliminate the cavity through the cavitation phenomena prediction.
- (2) Allocate the amount of work between an inducer and an impeller and determine how much the suction performance is affordable.
- (3) Design the flow passage to enter smoothly the impeller inlet without any internal disturbance.

When the designed head of an inducer is higher than the necessary of the ideal head, a problem about the overall turbopump efficiency falling comes up. Therefore, the inducer must be appropriately designed. A hub diameter of the inducer inlet should be designed to withstand the

structural loads and the axial load that occur in the transmission power of its one weight and the fluid acting on the hub side blade, and the design should be as small as possible without structural problems because of the suction performance improvement when a inlet area increases. An inducer tip diameter is determined considering the minimum required *NPSH* and the maximum suction specific speed and so on. An incidence angle is properly determined around $4^\circ \sim 10^\circ$ unless the incidence angle does not have a negative value from hub to tip. This range of the incidence angle suppresses the recirculation zone. The recirculation zone is caused by the static pressure decrease and an increased probability of the flow separation. A velocity triangle of the inducer inlet is determined through the design process as shown in Fig 1.5.

$$U_1 = \frac{\omega D_1}{2} \quad (1.1)$$

$$C_1 = \frac{Q}{A_1} = \frac{4Q}{\pi(D_{1t}^2 - D_{1h}^2)/\sin\theta_1} \quad (1.2)$$

$$W_1 = \sqrt{U_1^2 + C_1^2} \quad (1.3)$$

$$\beta_1 = \tan^{-1}(C_1/U_1) \quad (1.4)$$

$$\beta_{b1} = \beta_1 + i \quad (1.5)$$

$$\phi_1 = \frac{C_1}{U_1} \quad (1.6)$$

A blade length is determined after a blade number and a solidity are given.

$$s = \frac{L_{blade}}{P} = L_{blade} \frac{Z}{\pi D_1} \quad (1.7)$$

$$L_{blade} = \frac{s\pi D_1}{Z} \quad (1.8)$$

The inducer outlet must be made for the design head in order to improve the suction performance of the impeller and its maximum hydraulic efficiency of the inducer. Typically, the tip diameter of the inducer outlet is less than inlet diameter of the inducer because the inducer efficiency and the impeller size are able to reduce. The deviation angle is determined when the outlet blade angle is given. A velocity triangle of the inducer outlet is determined through the design process as shown in Fig 1.6. Finally, the mean line design method of the inducer is completed.

$$U_2 = \frac{\omega D_2}{2} \quad (1.9)$$

$$C_{m2} = \frac{Q}{A_2} = \frac{4Q}{\pi(D_{2t}^2 - D_{2h}^2)} \quad (1.10)$$

1.3 Problem description

The design methods for inducers have been studied since 1950s. A variety of parameters must be considered in the design of the turbopump inducer. These parameters include the optimum inlet diameter, the inlet blade angle, the design point incidence value, leading edge shape, and the blade number as well as the blade turning angle and structural design parameters. In conventional design method, helical inducers are commonly used for turbopump inducer applications. Several approaches were studied to improve suction performance or suppress instability related to cavitation phenomena using a variable lead design or applying a cambered bladed design to the inducer geometry.

Tsujimoto et al.(2001) and Yoshida et al.(2001) showed that a backward leading edge sweep suppressed both the development of cavities on the blade suction surface and the occurrence of cavitation instability such as alternate blade cavitation and rotating cavitation. Ashihara et al.(2002) applied the 3D inverse design method developed by Zangenh(2003) to inducer design and investigated the effects of loading distribution on inducer performance. They showed that zero-incidence with fore-loaded design could suppress inlet recirculation, keeping the required suction performance at the design flow. Ashihara et al.(2001) also showed in the study of 3D inverse design of liquid hydrogen rocket pump inducers that zero-incidence design suppressed rotation cavitation in the inducer when operating range, so it is necessary in investigate design trade-offs between suction performance at high flow and stability

at design to low flow conditions. Japikse(2001) reviewed some of design methods and practices used for inducer design and provided a brief overview of design considerations for inducer design including the evaluation of suction specific speed as a function of inlet blade angle and flow coefficient. The survey by Lakchminarayana(1982) on the fluid dynamics of inducer is well known and provides a lot of technical detail and much general overview of design performance. Although many efforts have been made to improve the design method, the experimental verification is essential because the cavitating flow is too complex to predict.

Researches confirm the differences in the performance and the efficiency for shape modifications and scale. Studies have also been carried out on the blade angle, tip clearance(Okita, 2009) and solidity (Hong, 2004) of design parameters. Kim et al(2012) reported the maximum head point about the tip clearance in Fig 1.7. Yoon et al.(2011) found that the diameter of the inducer inlet had the minimum $NPSH_r$ in Fig 1.8. The number of blade, which is one of the most important parameters, has a very significant impact on the head(Choi, 2009). This study reported that the head and the efficiency decreased as the blade number increase in Fig 1.9. O. Coutier et al(2012) studied the suction performance, and instabilities of the turbopump inducer for different bladed number inducers. However, in the above studies, the number of blade is simply changed with respect to the same axial length. In other words, not only is the number of the blade changed, but also the solidity changes at same time. Thus, as reported in these studies, this

effect makes it difficult to determine whether the influence is due to the blade number or the solidity. For this reason, in this study, the performance, the efficiency, and cavitation instabilities will be evaluated in which the different blade number and the different solidity.

1.4 Research objectives

The main purpose of this research is to investigate the performance and cavitation instabilities in the turbopump inducer with the effect of the blade number and the solidity. The detailed research objectives are as follows.

- (1) To study the effect of the blade number and the solidity on the head and the efficiency and analyze the reason why the differences occur.
- (2) To compare an empirical equation about the deviation angle, the efficiency, and the $NPSH_r$ (3% head drop point) with results applied the effects and recommend a new empirical equation.
- (3) To investigate cavitation instabilities focused on the cavitation inception and the further cavitation inception.



Fig. 1.1 KSLV-I

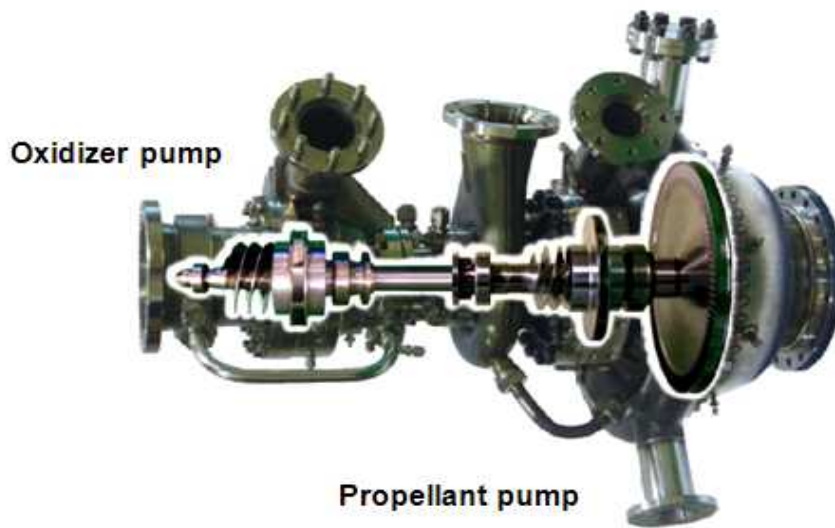


Fig. 1.2 Capability of 30,000 Kg Turbopump

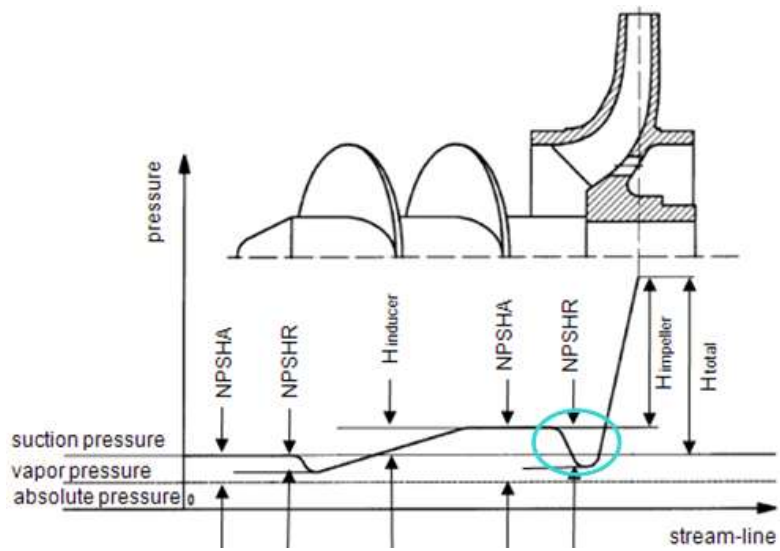


Fig. 1.3 Pressure equilibrium of the inducer design

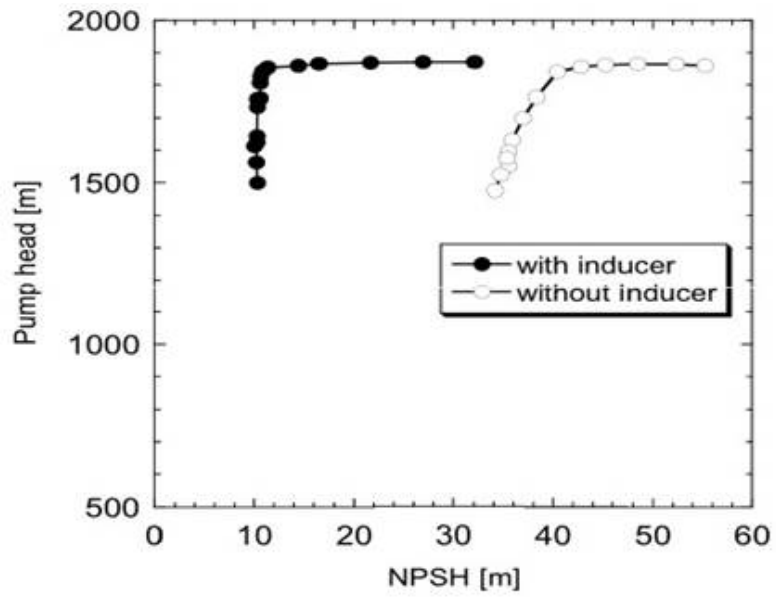


Fig. 1.4 Effect of the inducer on the cavitation performance

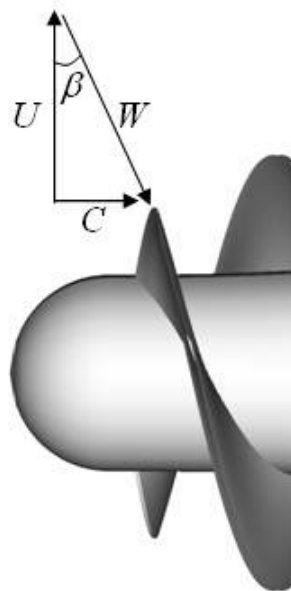


Fig. 1.5 Velocity triangle of the inducer inlet

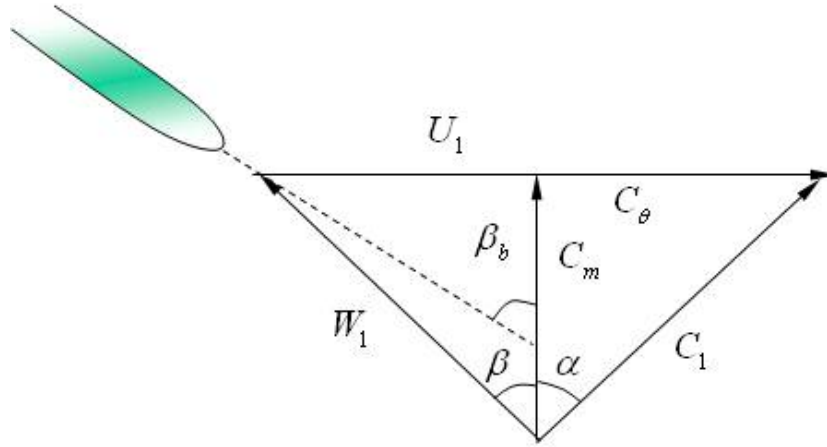


Fig. 1.6 Velocity triangle of the inducer outlet

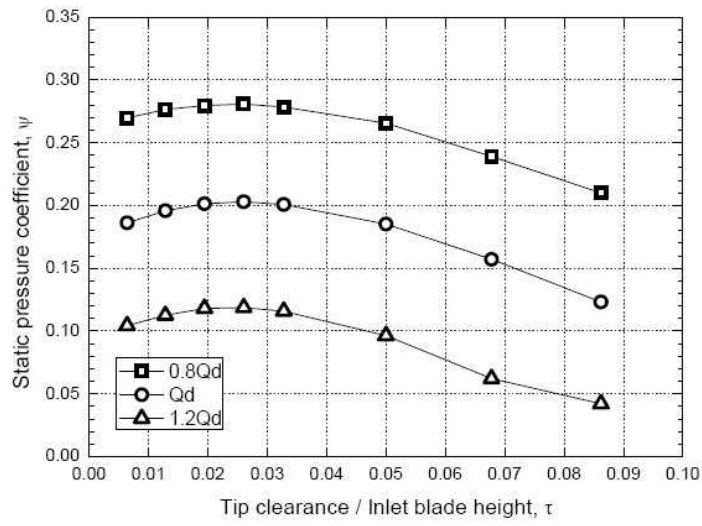


Fig. 1.7 Static pressure coefficients with respect to the tip clearance

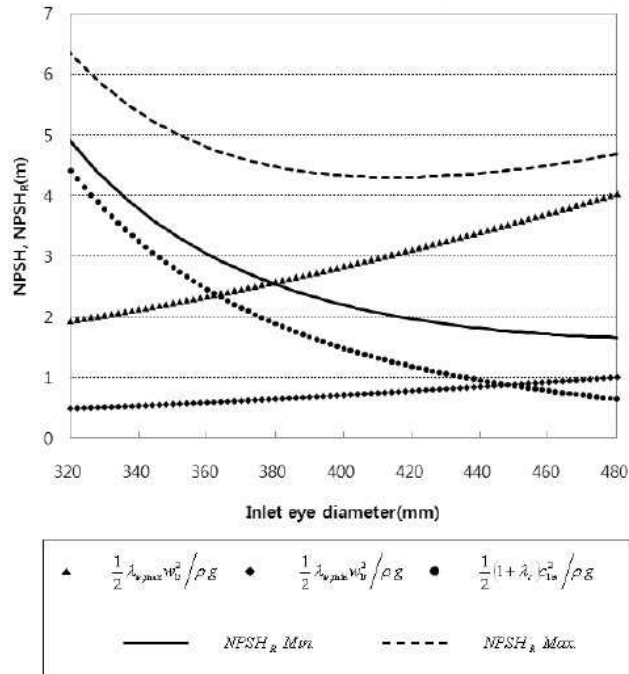


Fig. 1.8 $NPSH_r$ of the inducer

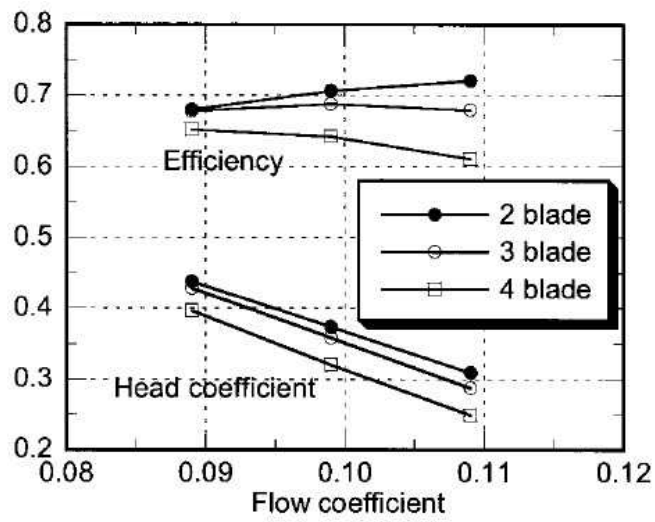


Fig. 1.9 Head and efficiency performance

Chapter 2. Research Method

2.1 Inducer Model

The basic model is a two bladed inducer, and the solidity is set at a ratio of 2(Z2s2). Adding only one blade with respect to the same axial length, the second is selected for comparison model(Z3s3). Finally, the third has three bladed with the same solidity of the basic inducer(Z3s2). Therefore, three kinds of inducers are designed. Fig. 2.1 shows three kinds of turbopump inducers. Specifications of the inducers are shown in Table 2.1. All three models are satisfied with the geometric similarity of the blade number and the solidity parameters, but the fluid dynamics similarity is not satisfied. Reynolds number is the most representative dimensionless number of the fluid dynamics. Brennen(1994) reported that the efficiency has no influence on the over 10^6 Reynolds number as shown in Fig 2.2. So it is seen that results reflect the geometric parameters without Reynolds number effect in this study.

2.2 Experimental analysis

The test facility used in the present study is shown in Fig 2.3, where the apparatus has a closed loop tunnel. The facility operates in

de-aerated water for the cavitation experiment test. The impurities in water are filtered out when it is supplied into the facility. A 30 kW alternative motor powered by a variable frequency controller was used to drive the inducer. The flow rate is measured by an electro-magnetic flow meter and controlled by the valve installed at a discharge pipe connected to a tank. The inlet pressure is controlled by a pressure control tank and a vacuum pump. All tests are conducted at 3,000 rpm(50 Hz rotating frequency) throughout the present study.

The details of test section and the locations of pressure measurement are shown in Fig 2.4. The test Section made by an acrylic plastic is transparent so that the cavity on the blade is able to be observed with a high speed camera. Pressure rise is measured by differential pressure transducer installed between the inlet and the outlet section of test inducers. A casing wall has 6 pressure taps to measure the axial distribution of static pressure. To analyze the unsteady cavitation phenomena, pressure transducers are flush-mounted located at the casing wall of two axial locations. Pressure fluctuations are obtained at a sampling rate of 2400 Hz. NI board and Labview commercial program are used for acquiring and collecting measurement signals. Experiments for cavitation performance are carried out at a constant value of the flow coefficient by continuously reducing the inlet pressure from atmospheric condition to the minimum allowable value.

Data from the pressure transducer and the torque meter is converted through the calibration. The calibration graph of the pressure transducer and torque meter are shown in Fig 2.5. To evaluate the measurement

uncertainty of data, the averaged data test did 100 times for 30 seconds and acquired the result. The measurement uncertainty of pressure data is ± 1.14 percent with 95 % confidence interval. The uncertainties of the torque and the mass flow rate are ± 0.51 percent and ± 0.48 percent, respectively. Results are obtained the reliability through repeated experiments for the three rotating speed as shown in Fig 2.6. The non dimensional performance curve is also obtained the reliability of the similarity as shown in Fig. 2.7. In case of the 3000 rpm, the pressure rise value of the high flow mass rate decreased compared with other cases. This discrepancy is the reason why the cavitation occurred.

2.3 Numerical analysis

For this research, numerical analysis is conducted with a commercial package, ANSYS-CFX 11.0. This code is widely used to predict the performance and the flow structure of turbomachinery in academy and industry fields. This solver is based on three-dimensional Navier-Stokes equations solved by finite volume method with hybrid unstructured grid

The numerical calculation is conducted on the domains as shown in Fig. 2.8. The domains include the intake, the inducer, the impeller and the vaneless diffuser. Frozen-rotor conditions are used between the rotating domain and the stationary domain. This model is very useful that the frame of reference pitch is changed but the relative orientation of the components across the interface is fixed. The two frames of

reference connect in such a way that they each have a fixed relative position throughout the calculation. If the frame changes the appropriate equation transformations are made. If the pitch changes, the fluxes are scaled by the pitch change. This model produces a steady state solution to the multiple frame of reference problem, with some account of the interaction between the two frames. The quasi-steady approximation involved becomes small when the through flow speed is large relative to the machine speed at the interface. Frozen Rotor analysis is most useful when the circumferential variation of the flow is large relative to the component pitch. This model requires the least amount of computational effort of the three frame change/mixing models.

The inlet boundary conditions are the total pressure, total temperature, which correspond to the atmospheric conditions. The outlet boundary condition is the mass flow rate where the operating condition was adjusted. The mass flow rate is imposed on the boundary with Neumann condition by iteratively scaling the velocity at each node. Adiabatic and non-slip conditions are applied to the solid walls.

To find a reasonable turbulence model for the flow analysis in the turbopump inducer, numerical calculations of static pressure distributions from inlet to outlet using k-epsilon model and shear stress transport (SST) model are compared with the experiment result under non-cavitation condition at design mass flow rate. Both models are nearly same and good agreement with the experiment result. The shear stress transport(SST) model is selected since this model is more accurate at the inducer leading edge. The SST model is designed to give a highly

accurate predictions of the onset and the amount of flow separation under adverse pressure gradients by the inclusion of transport effects into the formulation of the eddy-viscosity. This results in a major improvement in terms of flow separation predictions. Furthermore, this model is recommended for high accuracy boundary layer simulations. To benefit from this model, a resolution of the boundary layer of more than 10 points is required.

About 3,000,000 numerical cells per full blade passages with a structured H-type mesh with O-grid around the blade are selected after numerical uncertainty tests that showed no loss in accuracy as shown in Fig 2.9. Ten cells are sufficient for the tip clearance since it is found by Hwang(2013) that the viscosity in the gap had little effect on the overall pattern of the tip leakage flow.

Tests for grid dependency, and turbulence model are described in Fig 2.10 and Fig 2.11 in detail. 8 CPUs and 16 CPUs of 2.5 GHz with 32GB RAM were used for the steady calculation and the cavitation calculation respectively.

2.4 Comparison with measured data

When carrying out the experiment test and the numerical calculation, a direct comparison of results is difficult because of the different definitions and the measurement condition for the variables in their own method. Therefore, it is defined that the criteria, the measurement

position, and the average method are required under the same conditions in order to compare the identical results of both experiment test and the numerical calculation. The flow coefficient and the pressure rise coefficient are defined with the inducer tip speed as

$$\phi = \frac{Q}{AU_t} \quad (2.1)$$

$$\psi = \frac{gH_t}{U_t^2} \quad (2.2)$$

Where, H_t and A are the total head and the area of the inducer inlet. The total head is selected so that this value is needed to evaluation and predict for the deviation angle, and the empirical equation. The total pressure refers to the sum of the static pressure and the dynamic pressure. In numerical calculation, both values are used by the mass average in the radial and circumferential direction. However, the velocity for determining the dynamic pressure is used in the results of the 1D since it is difficult to measure in the experiment test. The relative velocity angle for the radial direction is used from the forced vortex method. Fig 2.12 and Fig 2.13 show distributions of the relative velocity angle and the tangential velocity. Fig 2.14 shows the axial velocity distribution from hub to tip using the radial equilibrium equation.

$$r \tan \beta = K_1 \quad (2.3)$$

$$C_\theta = K_2 \quad (2.4)$$

$$C_x \frac{dC_x}{dr} + \frac{C_\theta}{r} \frac{d(rC_\theta)}{dr} = 0 \quad (2.5)$$

$$\frac{\partial p}{\partial r} = \rho \frac{C_\theta^2}{r} \quad (2.6)$$

The static pressure is able to be measured by the accurate measurement because the pressure data is directly obtained by the pressure transducer. However, one thing is considered as part of the location. The static pressure is measured at the casing wall, which means that both are also the different data compared to the averaged value. Therefore, the averaged static pressure of the experiment test is used from 1D Navier–Stokes equation. Fig 2.15 shows the location obtained the static pressure for the head at the inducer outlet, and Fig 2.16 shows the graph of the static pressure distribution from hub to tip, the mass averaged static pressure, and the experiment static pressure. Although the result of the experiment test was higher than that of the numerical calculation, the gap was not a big difference. The deviation between the numerical calculation dynamic head and the experiment head was 22.13 % to the static head. This correction was applied by those ratios.

$$P_t = P_{corr} + \frac{1}{2} \rho \bar{C}_{1D}^2 \quad (\text{EXP}) \quad (2.7)$$

$$H_t = \frac{P_t - P_{t,in}}{\rho g} \quad (\text{EXP}) \quad (2.8)$$

$$\bar{P}_t = \bar{P} + \frac{1}{2} \rho \bar{C}_{cfD}^2 \quad (\text{CFD}) \quad (2.9)$$

$$H_t = \frac{\bar{P}_t - P_{t,in}}{\rho g} \quad (\text{CFD}) \quad (2.10)$$

The efficiency is defined as

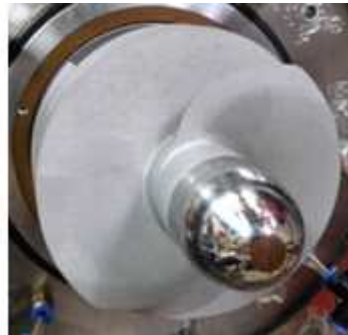
$$\eta = \frac{\rho g H Q}{T \omega} \quad (\text{EXP}) \quad (2.11)$$

$$\eta = \frac{g H}{U_2 C_{\theta 2}} \quad (\text{CFD}) \quad (2.12)$$

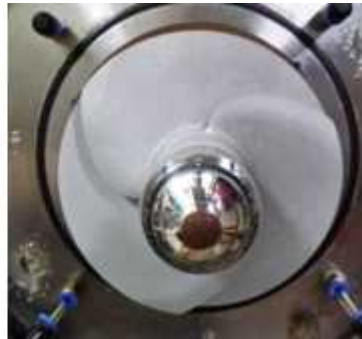
Where, T and ω are the torque and the angular velocity. The torque data was measured by the torque transducer in the experiment test, and the torque data of the numerical calculation used in the momentum value. The tip speed and the circumferential velocity is the same value to the torque data from Euler-turbine equation. The discrepancy about those values will be more discussed later in Chapter 3.



(a)



(b)



(c)



Fig. 2.1 Inducer: (a) Z2s2; (b) Z3s3; (c) Z3s2

Table 2.1 Specification of Inducer.

Inducer	Blade Number	Solidity
Z2s2	2	2
Z3s3	3	3
Z3s2	3	2

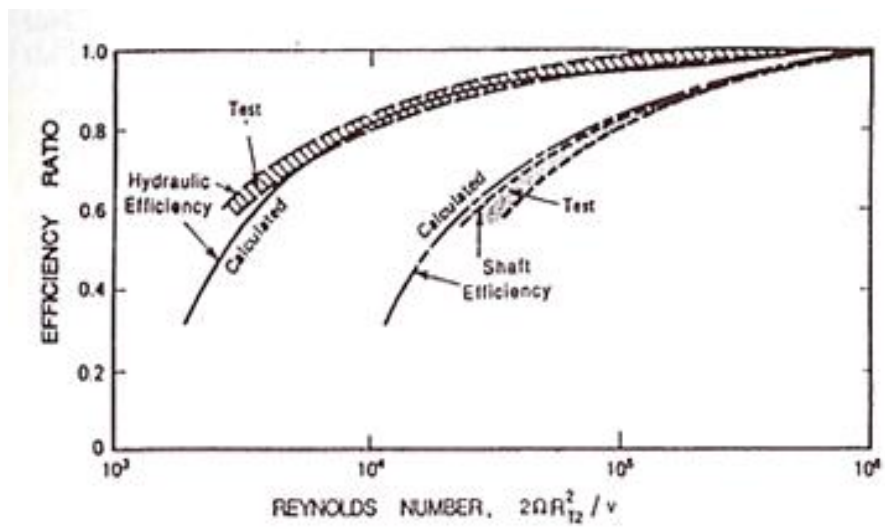


Fig. 2.2 Effect of Reynolds number on the efficiency

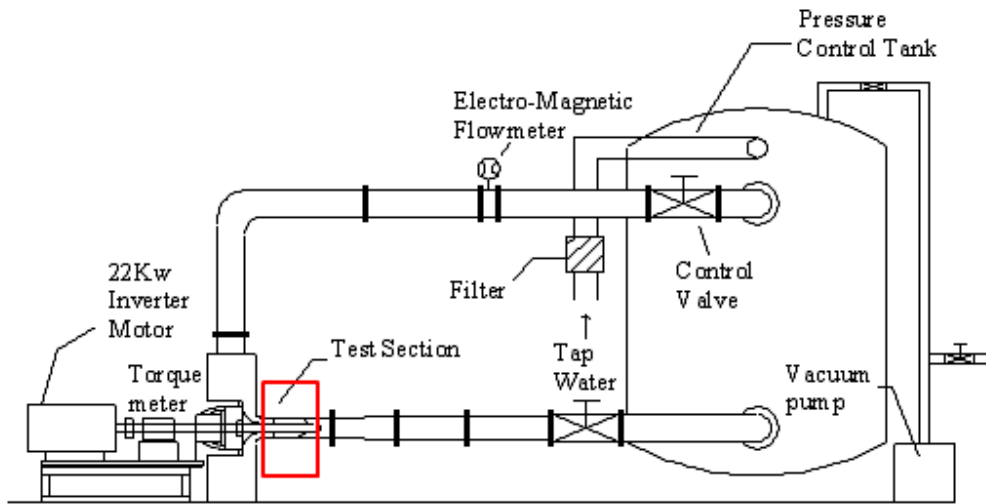


Fig. 2.3 Schematic of the test facility

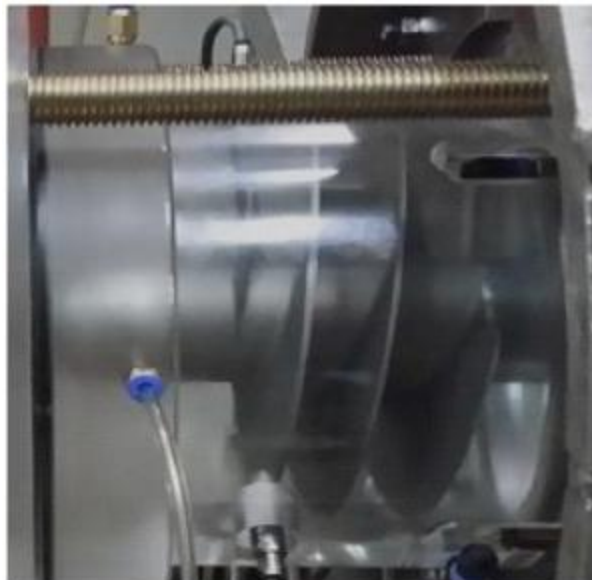
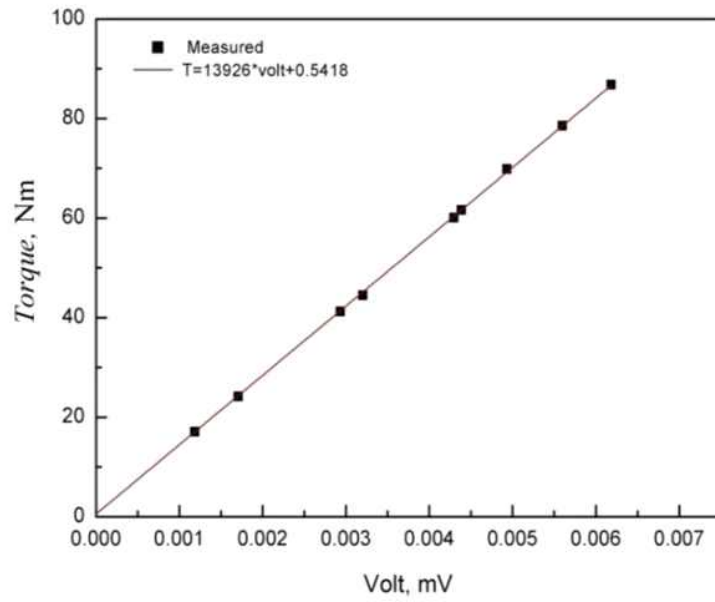
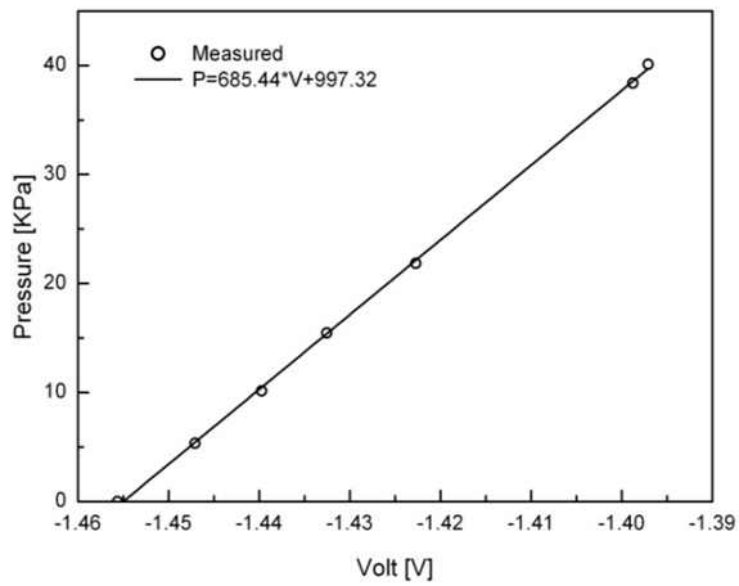


Fig. 2.4 Test section of the inducer



(a)



(b)

Fig. 2.5 Calibration: (a) for torque transducer; (b) for pressure transducer

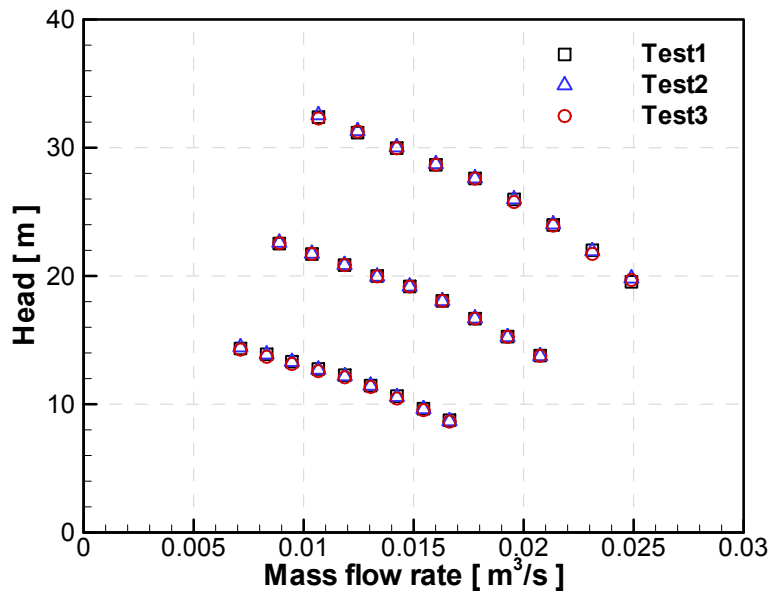


Fig. 2.6 Validation of the repeatability experiment test

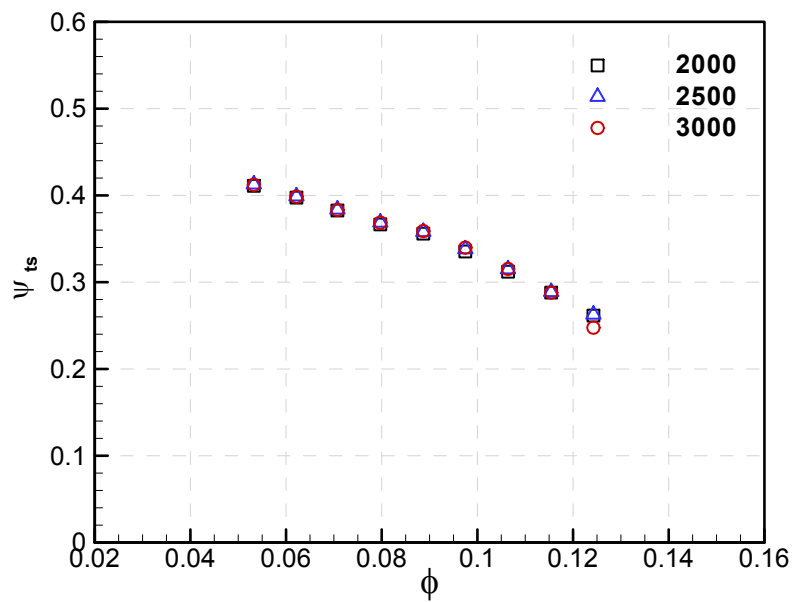


Fig. 2.7 Non dimensional pressure rise performance

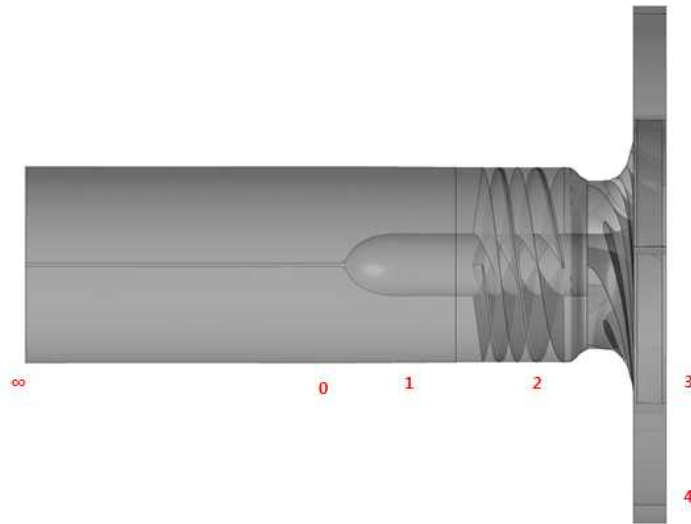


Fig. 2.8 Computational domain for a turbopump

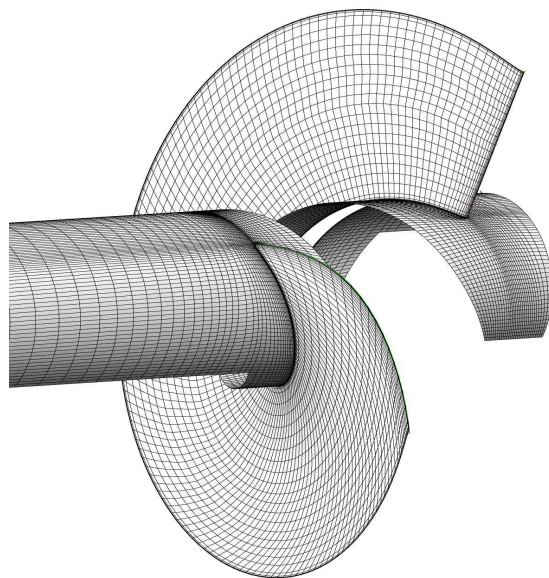


Fig. 2.9 Computational grid of an inducer

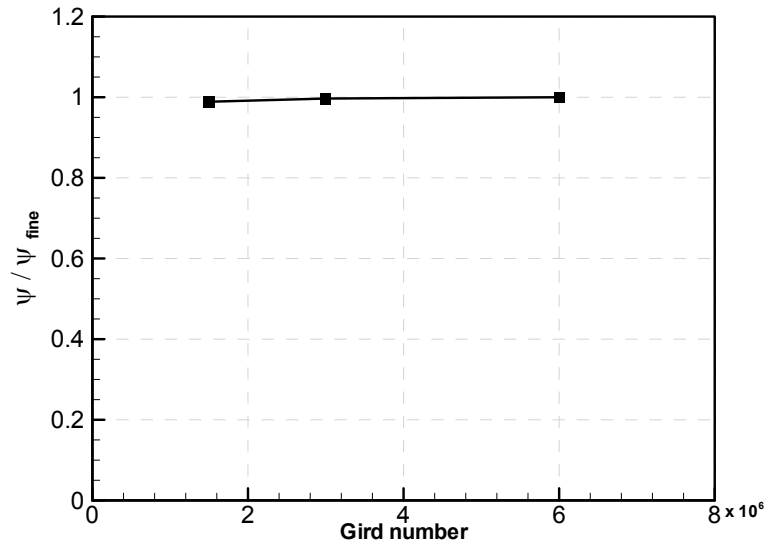


Fig. 2.10 Grid dependency test: Comparison of the static pressure coefficient

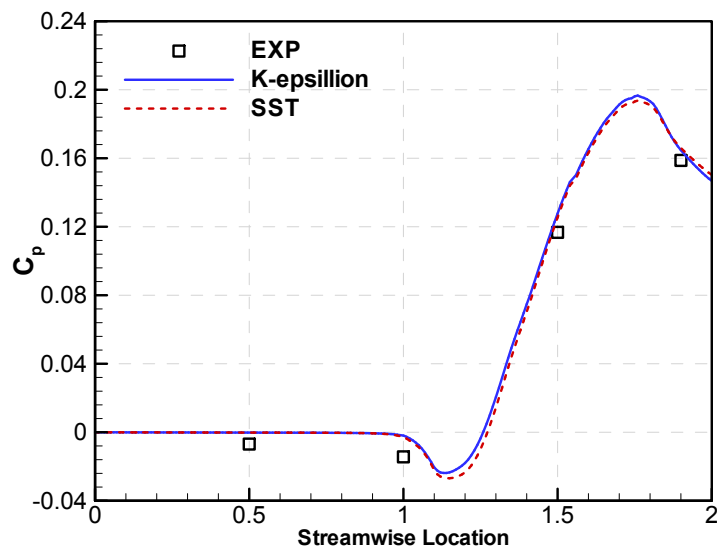


Fig. 2.11 Comparison of the turbulence model for the static pressure coefficient

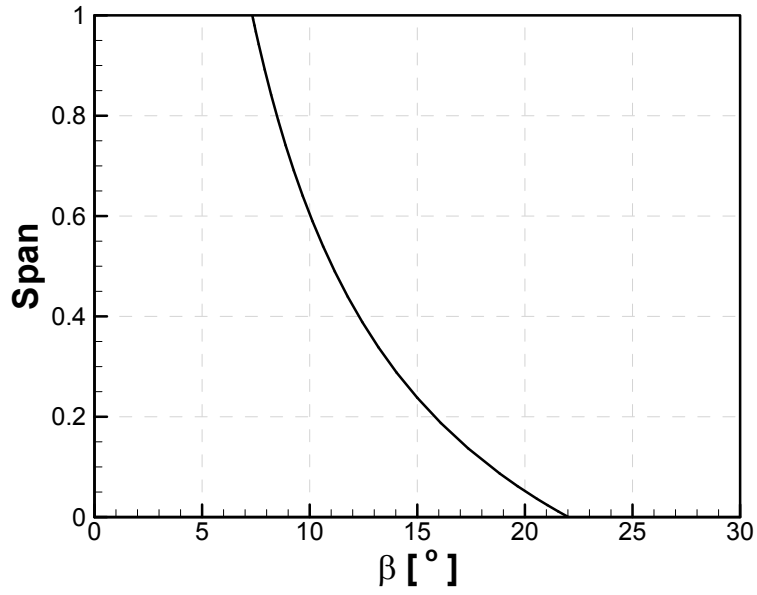


Fig. 2.12 Relative velocity distributions from hub to tip

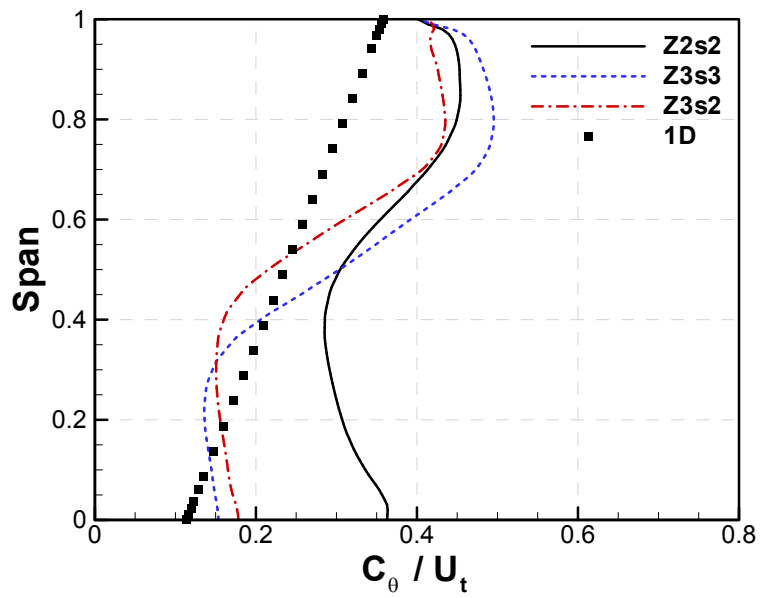


Fig. 2.13 Tangential velocity distributions from hub to tip

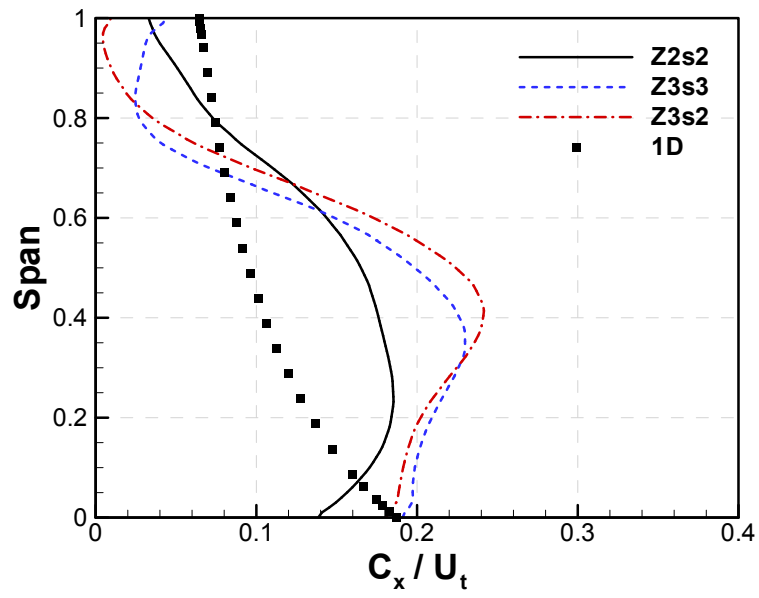


Fig. 2.14 Axial velocity distributions from hub to tip

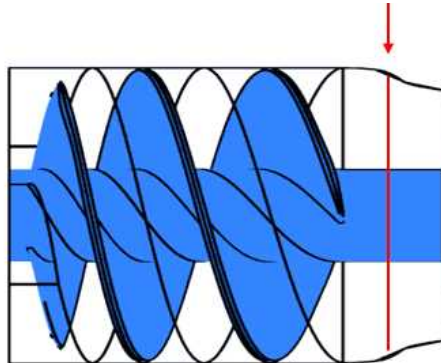


Fig. 2.15 Location of the data measurement

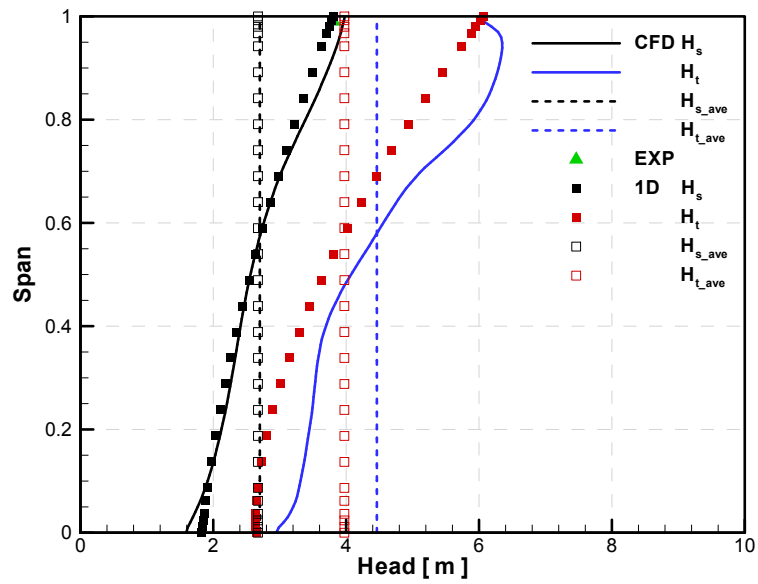


Fig. 2.16 Comparison the static head and the dynamic head at inducer outlet

Chapter 3. Hydraulic Performance

3.1 Pressure rise

Fig 3.1 shows the pressure rise performance(a) of inducers in non cavitating condition, in which the pressure rise was evaluated from the difference between the inlet total pressure and the outlet total pressure. As mentioned earlier in Chapter 2, it was adjusted through the correction of the pressure values applied the average effect and the dynamic head from 1D velocity. The difference between the experiment test and the numerical calculation was reduced by the correction(b). First, the total pressure rise of the Z3s3 experiment test was 12.75 % smaller than that of Z2s2 at design mass flow rate. ($\phi = 0.101$) This was confirmed by the results of an existing study(Choi, 2009). However, the total pressure rise of Z3s2 decreased by 18.74 % less than that of Z2s2. In numerical calculation, the total pressure rise curves of Z3s3 and Z3s2 were 16.13 % and 19.56 % smaller than that of Z2s2 at design mass flow rate, respectively. It seems that the only blade number effect is proved compared with Z2s2 and Z3s2.

The tendency of the deviation was the same among cases from a low mass flow rate to a high mass flow rate in numerical calculation. However, The result of the experiment test was different. In Z3s3 case, the pressure rise curve approached the Z3s2 at a low mass flow rate,

but the Z2s2 case at a high mass flow rate. As a result, the pressure rise curves of the experiment test and the numerical calculation among the three cases have a similar trend. The result of Z2s2 was the highest, and the result of Z3s2 was the lowest.

3.2 Work coefficient

For an inducer or impeller running at angular velocity, the rate at which the inducer does work on the fluid is

$$\tau_A w = \dot{m} (U_2 C_{\theta 2} - U_1 C_{\theta 1}) \quad (3.1)$$

Thus, the work done on the fluid per unit mass or specific work is

$$\Delta W_p = \frac{\dot{W}_p}{\dot{m}_p} = U_2 C_{\theta 2} - U_1 C_{\theta 1} \quad (3.2)$$

This equation is referred to as Euler's pump equation. The work coefficient is the dimensionless number of the work to fluid.

For $C_{\theta 1}$ is a zero,

$$\psi_0 = \frac{g}{U_2^2} (U_2 C_{\theta 2} - U_1 C_{\theta 1}) = \frac{g C_{\theta 2}}{U_2} \quad (3.3)$$

$$\psi_0 = \frac{\psi}{\eta} \quad (3.4)$$

The work coefficient meaning the theoretical head is related to the efficiency which means that it was neglected by disk friction, cavity leakage, and recirculation work and so on. The work coefficient is also dependent the slip factor or the deviation angle.

The torque data was measured by the torque transducer in the experiment test, and the torque data of the numerical calculation was obtained in the momentum value, Fig 3.2 shows the comparison of the torque and the work coefficient. For the numerical calculation, the work coefficient was used the theoretical circumferential velocity considering the deviation angle. For the experiment test, the work coefficient was obtained by the ratio of the efficiency to the pressure rise coefficient. Both results were in nominal range without a significant difference. As viewed in the overall mass flow rate, the negative slope was a constant. The value of Z2s2 was the highest and then, the value of Z3s3 and Z3s2 were followed.

3.3 Efficiency

Fig 3.3 shows the efficiency performance. The value of Z2s2 was the highest and then, the value of Z3s2 and Z3s3 were followed. In Z3s3 case, the efficiency of the experiment test was 10.1 % smaller than that of Z2s2 at design mass flow rate. ($\phi = 0.101$) However, the efficiency of Z3s2 decreased by 4.81 % less than that of Z2s2. In numerical calculation, the efficiency curves of Z3s3 and Z3s2 were 7.78 % and 4.84

% smaller than that of Z2s2 at design mass flow rate, respectively. It seems that those results were different in the result of the pressure rise performance trend. Fig 3.4 shows the error range of the experiment efficiency applied the accuracy of the pressure transducer. Even considering a margin of the error, it was reliable that the tendency of the efficiency using the experiment test was no change.

3.4 Comparison of the deviation angle and the circumferential velocity

It was examined that effects of the blade number and the solidity on the pressure rise, the work coefficient, and the efficiency. In this chapter, the reason of those differences will be evaluated by fluid characteristics through the numerical calculation. First of all, the diameter was design to reduce after the trailing edge. Due to the this shape, flow velocity was changed. So this impact was investigated about the only Z2s2 case. Three positions were selected from the trailing edge to the impeller inlet. Fig 3.5 shows location of three position. Fig 3.6 and Fig 3.7 show the distribution of the axial velocity and the relative circumferential velocity in the radial direction. The axial velocity was faster because the area of the passage reduced. The velocity at hub and mis span was well represented. However, the velocity at tip was no big difference due to the no-slip condition effect on the wall. The relative circumference velocity was faster from hub to tip and getting slower towards the

inducer outlet. This phenomenon seems that the inducer does not work to the fluid because there is not a inducer blade and the impeller is set up after the inducer. Fig 3.8 shows the deviation angle distributions in radial direction. The deviation angle is defined as follows:

$$\delta = \beta - \beta_b \quad (3.5)$$

which β and β_b are the flow angle and the blade angle. It can be found that the deviation angle gradually decreases considering the triangle velocity. Fig 3.9 shows the circumferential velocity from hub to tip. It was respected by the deviation angle distribution. Fig 3.10 and Fig 3.11 show the deviation angle in radial direction and the averaged value at position A. Fig 3.10 represents the effect of the blade number. Both cases were large at hun and small at tip. The mass averaged deviation angle of Z3s2 was smaller than that of Z2s2. Fig 3.11 represents the comparison of the solidity effect. The mass averaged deviation angle of Z3s2 was larger than that of Z3s3. These trend was satisfied by the empirical rule. Fig 3.12 shows the averaged deviation angle at position B. The tendency of three cases was changed compared to the result of the position A(a). In this study, the position B(b) for the deviation angle evaluation was selected under same condition for the comparison because the location of the pressure transducer was the position B in the experiment test. Fig 3.13 shows the circumferential velocity at position B(b). These trends were the same with the trends of the deviation angle distribution.

3.5 Comparison of the head

In general, the inducer head is increased in proportion to the circumferential velocity. Therefore, the head was determined by the difference in the circumferential velocity. Fig 3.14 shows the head distribution applied the effect of the blade number compared with Z2s2 and Z3s2. The head of Z2s2 rose earlier after leading edge, and then, the head of Z3s2 rose at the 20% chord length of the blade. Both reached the head peak just after the trailing edge at position A, and the head decreased after position A. Both slopes were smoothly changed the positive to the negative. However, the negative slopes between Z2s2 and Z3s2 were different. Fig 3.15 shows the head distribution applied the solidity effect compared with Z3s3 and Z3s2. The head of Z3s3 and Z3s2 rose in parallel. It can be seen that the reason of the head rise location is not the solidity but the blade number. In Z3s3 case, the head rose very sharply and also dropped immediately. This phenomenon seems to relate to the deviation angle. The negative slopes for two cases were equal to each other after the trailing edge. So it can be seen that they have the same characteristics. Fig 3.16 shows the head distribution of the three cases. Fig 3.17 shows the static head distribution of the three cases for the numerical calculation and the experiment test. The static head of the numerical calculation was measured on the blade surface, and that of the experiment test was measured at the casing wall, so both results were not exactly values. However, this trend was known the head characteristics.

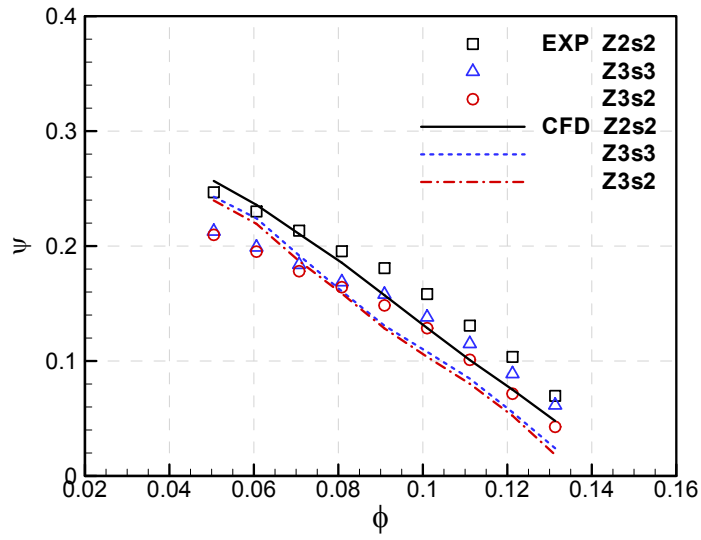
3.6 Comparison of the relative total pressure

The role of the inducer driven by the motor is to transport the work to the fluid. However, the inducer seems to stop in the relative frame. So the fluid passes through the inducer. In this case, hub, tip, and between the blade and the next blade is like a pipe. Therefore, the relative total pressure loss of the fluid occurs. The total pressure drop occurs when frictional forces, caused by the resistance to flow, act on a fluid as it flows through the tube. The main determinants of resistance to fluid flow are fluid velocity through the pipe and fluid viscosity. Pressure drop increases proportional to the frictional shear forces within the piping network. A piping network containing a high relative roughness rating High flow velocities and high fluid viscosities result in a larger pressure drop across a section of the inter flow. The low velocity will result in lower or no pressure drop. Fig 3.18 shows the relative total pressure loss coefficient at the mid span. the relative total pressure loss coefficient is defined as

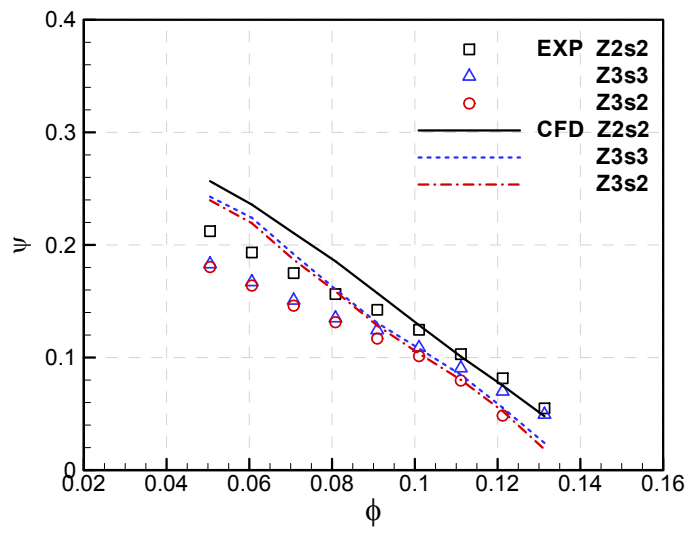
$$K = \frac{P_{trel\ in} - P_{trel}}{\frac{1}{2}\rho U_t^2} \quad (3.6)$$

The relative total pressure loss for all three cases increased. Especially, the loss of Z3s3 and Z3s2 was bigger and continued to the impeller inlet. Fig 3.19 shows the relative total pressure loss coefficient

at the 90 % span. The loss was getting increase passing the passage. Furthermore, the loss at the pressure surface was bigger than that of the suction surface. The loss at mid span propagated to the impeller along only streamline. However, the loss at 90 % span propagated to the impeller along not only streamline direction but also the circumferential direction. Fig 3.20 shows the radial and tangential mass averaged relative total pressure loss coefficient for three cases. The loss of Z3s3 was the biggest everywhere. Fig 3.21 shows the relative velocity distributions at the inducer outlet for the three cases. Unlike the relative velocity gradient of Z2s2, those of Z3s3 and Z3s2 were more glaringly obvious. It can be seem that the mixing loss is also bigger. Those loss characteristics influenced on the efficiency. Therefore, the efficiency of Z3s3 was the lowest compared with other cases, even though the pressure rise performance of Z3s3 was higher than that of Z3s2.

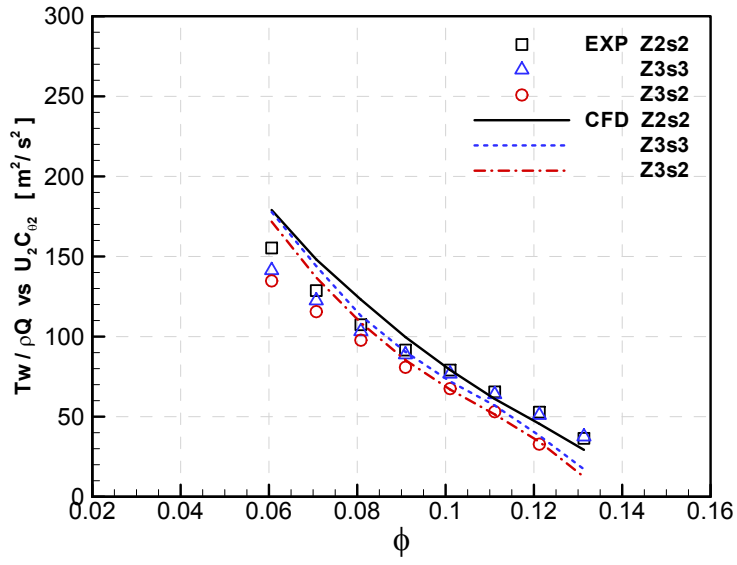


(a)

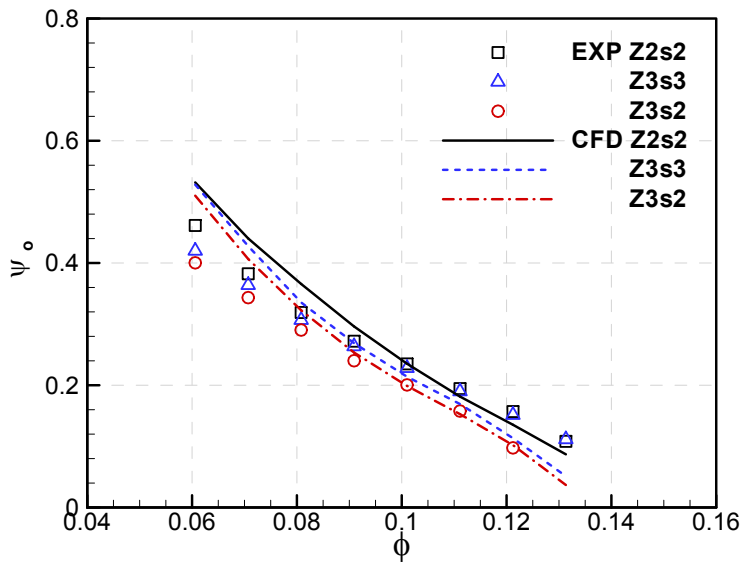


(b)

Fig. 3.1 Pressure rise performance: (a) w/o correction; (b) w/ correction



(a)



(b)

Fig. 3.2 (a) Torque; (b) Work coefficient

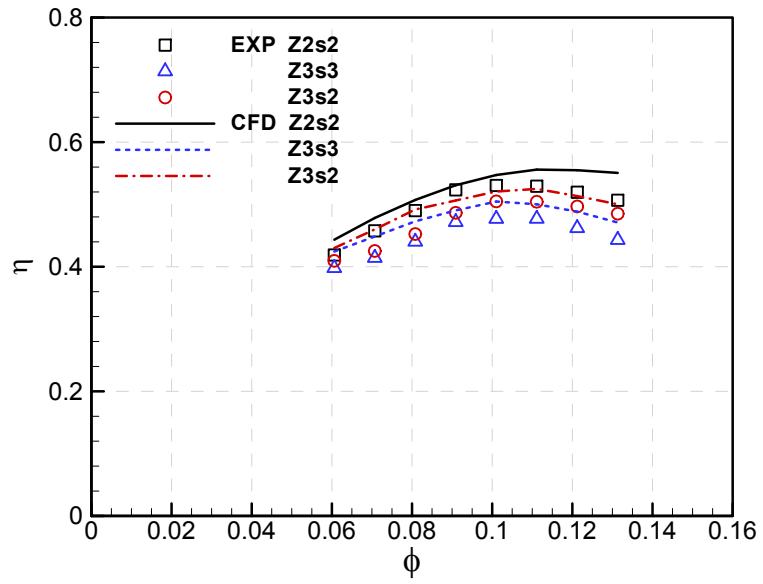


Fig. 3.3 Efficiency performance

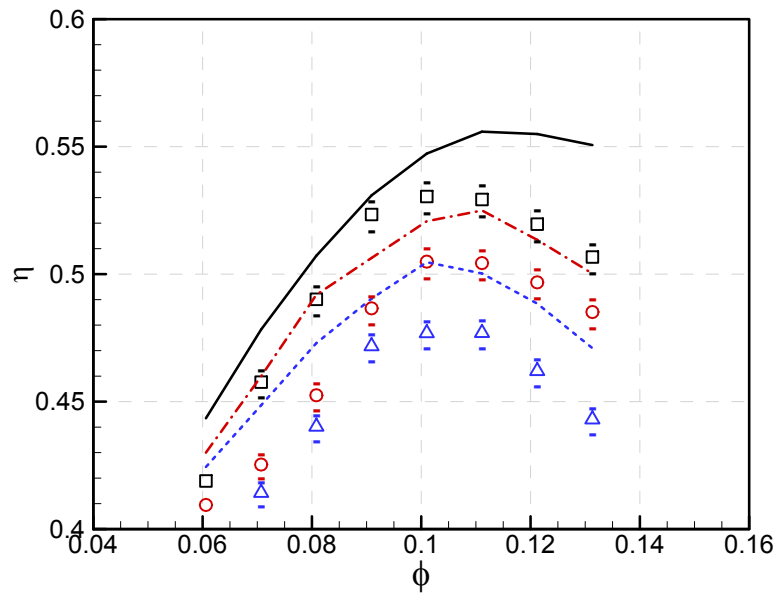


Fig. 3.4 Data uncertainty for the efficiency

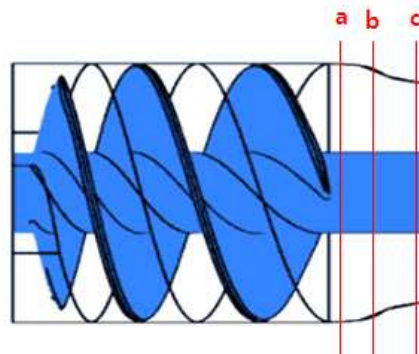


Fig. 3.5 Location of the inducer outlet

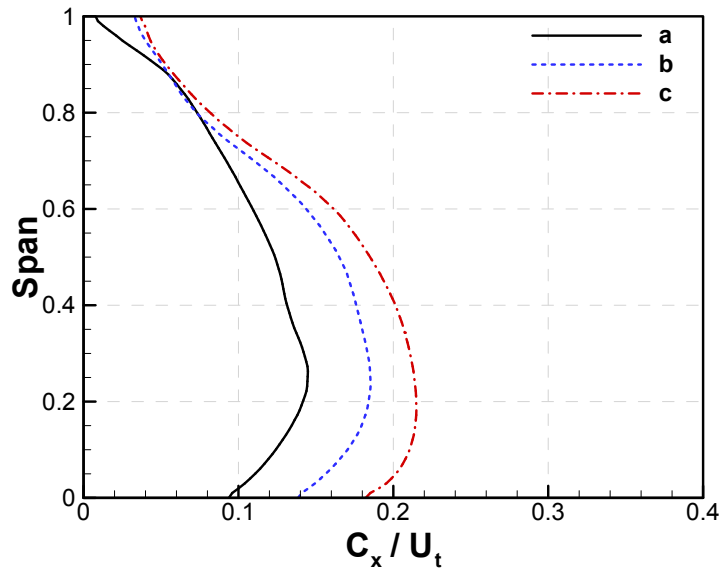


Fig. 3.6 Axial velocity distribution for Z2s2

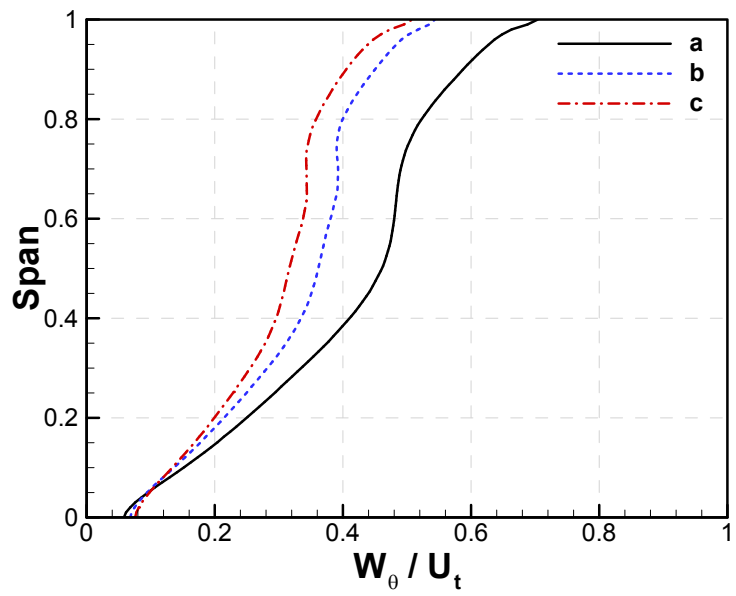


Fig. 3.7 Relative circumferential velocity distribution for Z2s2

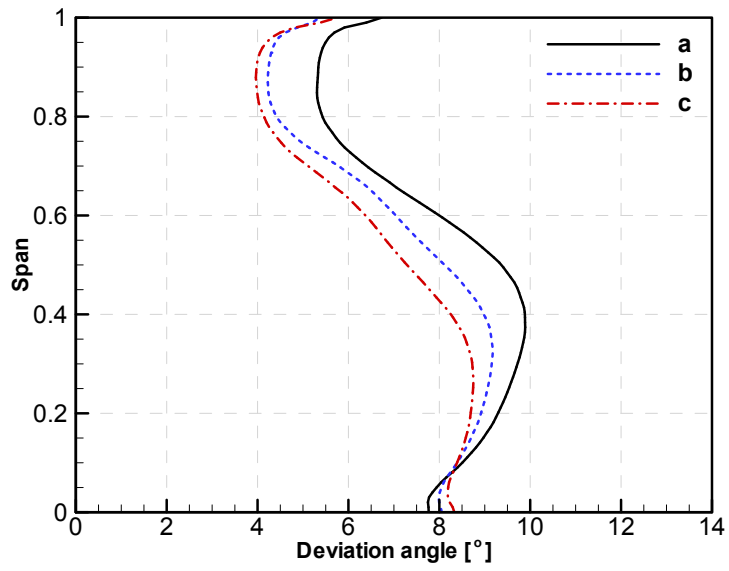


Fig. 3.8 Deviation angle distribution for Z2s2

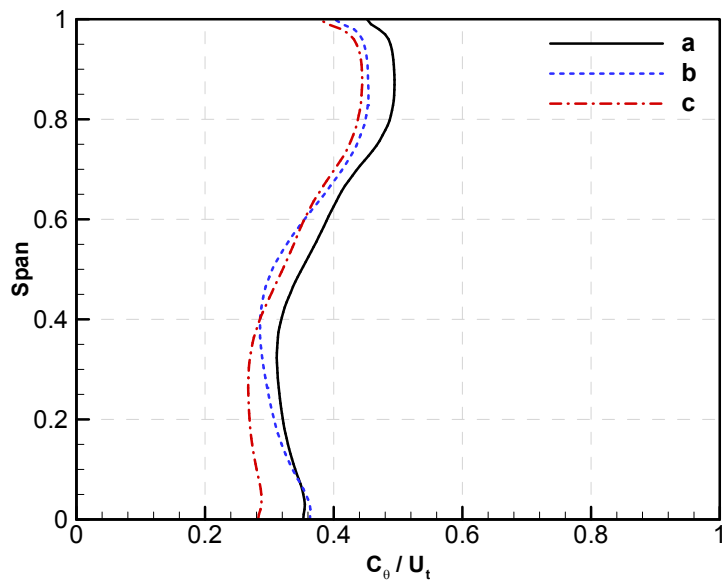


Fig. 3.9 Circumferential velocity distribution for Z2s2

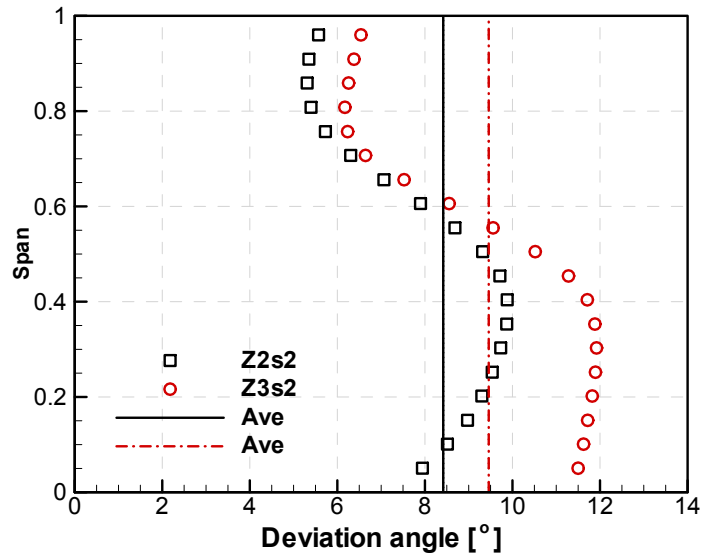


Fig. 3.10 Effect of the blade number on the deviation angle distribution at location A

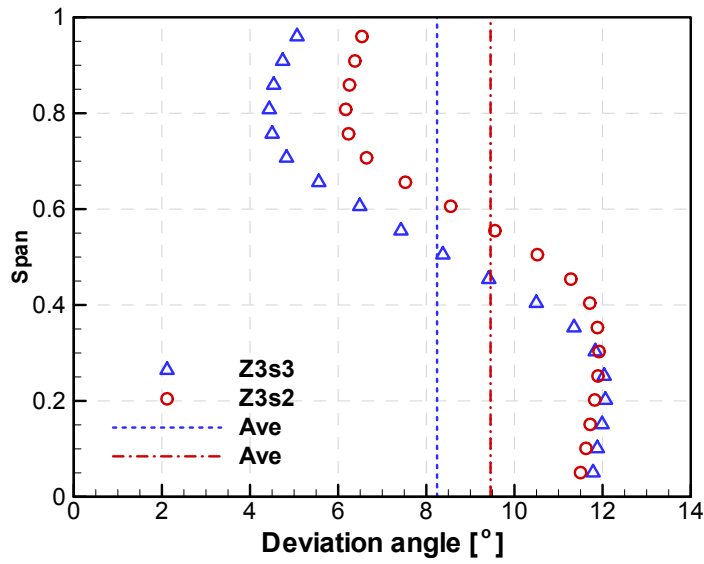
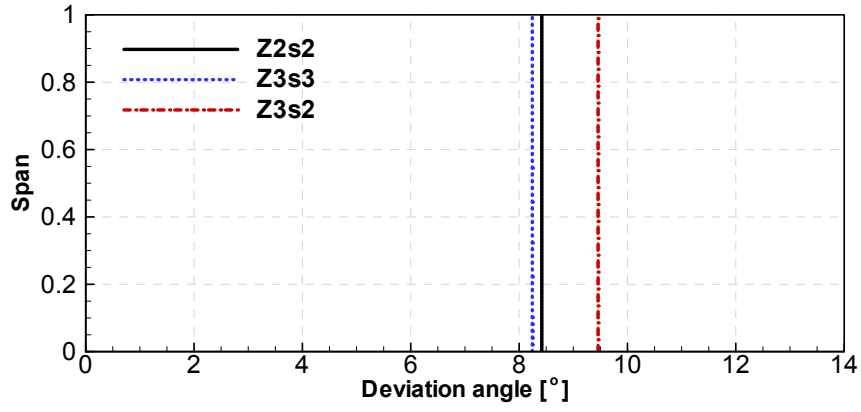
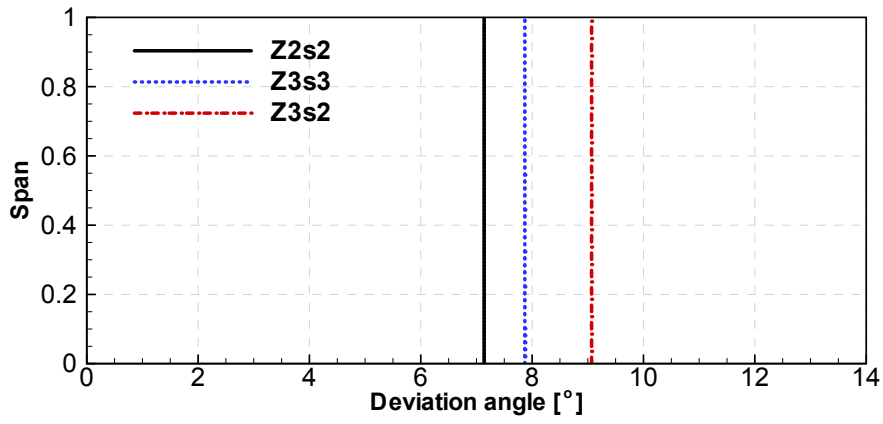


Fig. 3.11 Effect of the solidity on the deviation angle distribution at location A

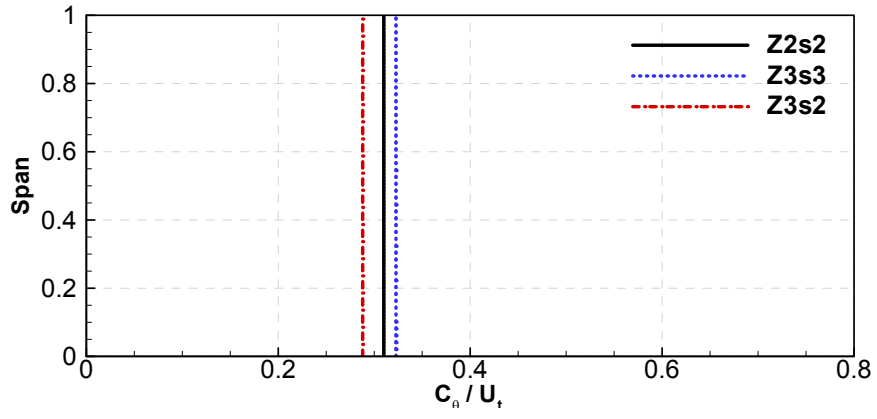


(a)

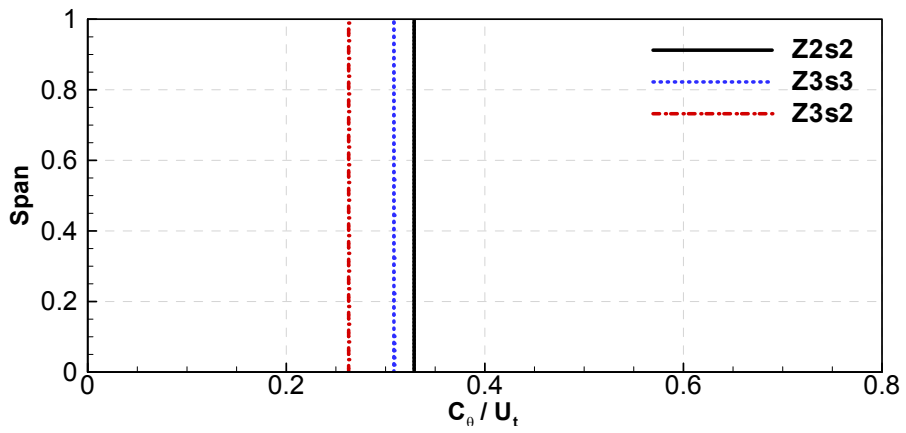


(b)

Fig. 3.12 Deviation angle distribution: (a) at location A; (b) at location B



(a)



(b)

Fig. 3.13 Circumferential velocity distribution: (a) at location A; (b) at location B

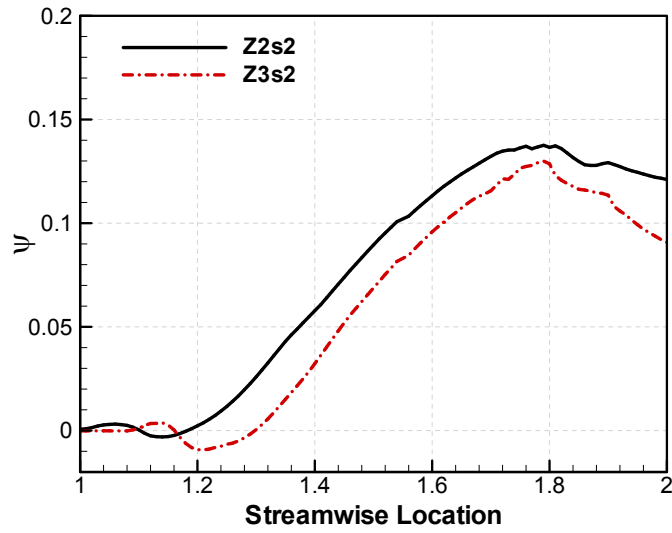


Fig. 3.14 Effect of the blade number on the head distribution of the inducer

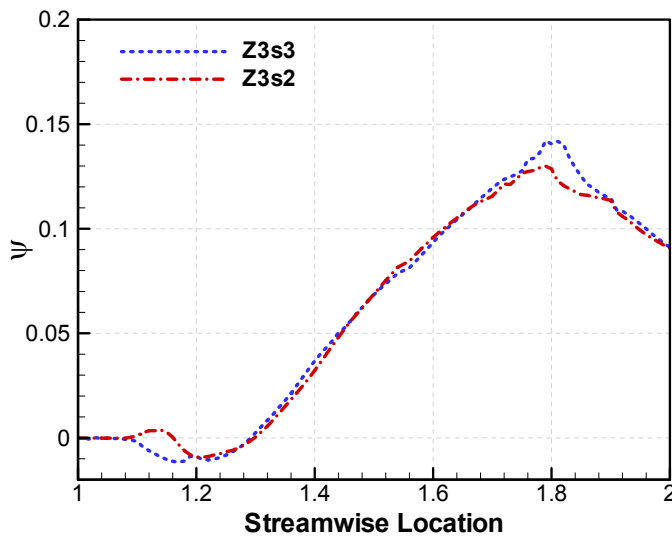


Fig. 3.15 Effect of the solidity on the head distribution of the inducer

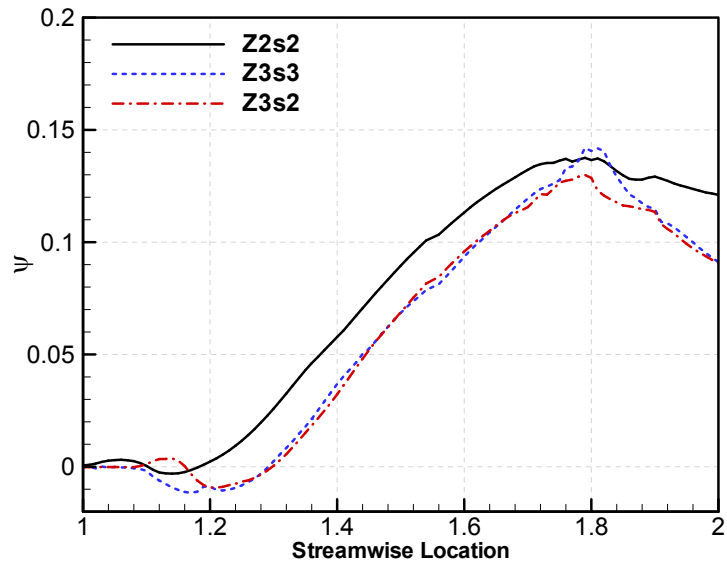
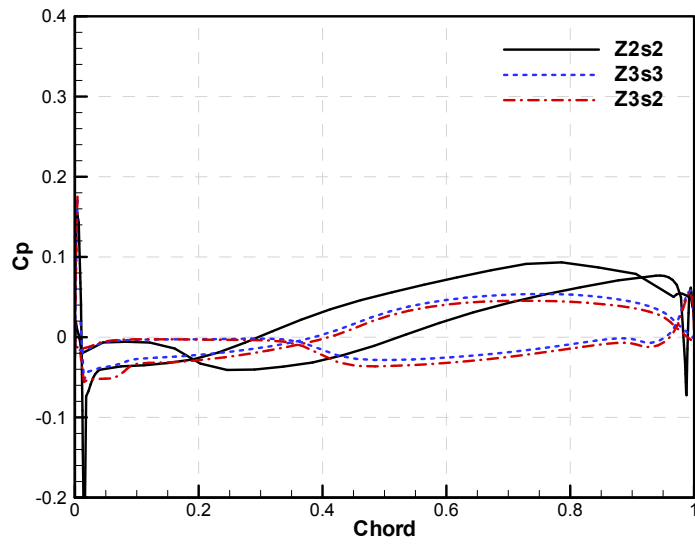
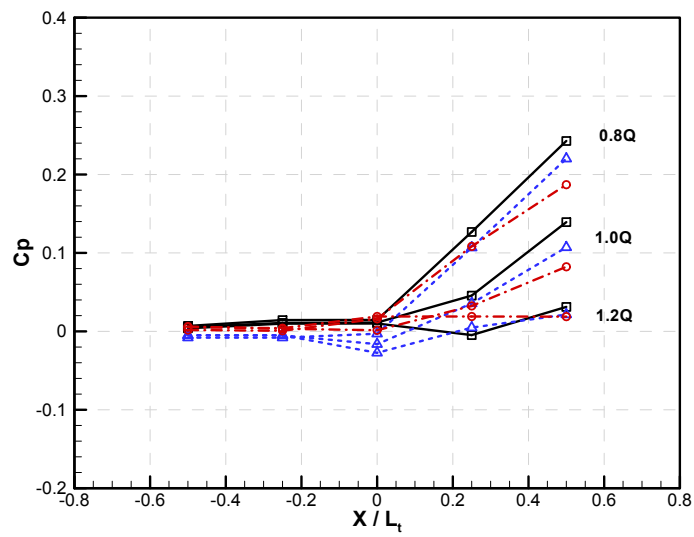


Fig. 3.16 Head distribution of the inducer for three cases



(a)



(b)

Fig. 3.17 Static head distribution: (a) CFD; (b) EXP

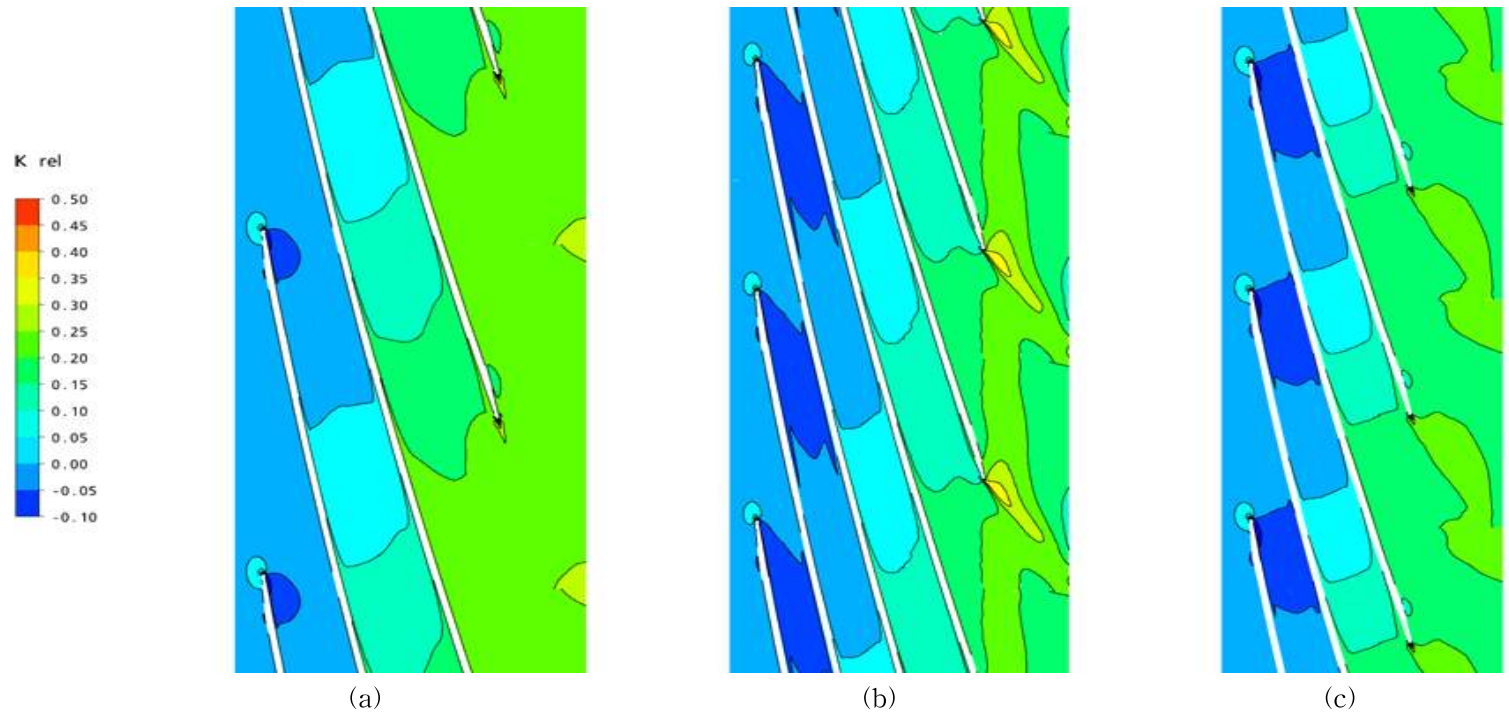


Fig. 3.18 Relative total pressure loss characteristic at mid span: (a) Z2s2; (b) Z3s3; (c) Z3s2

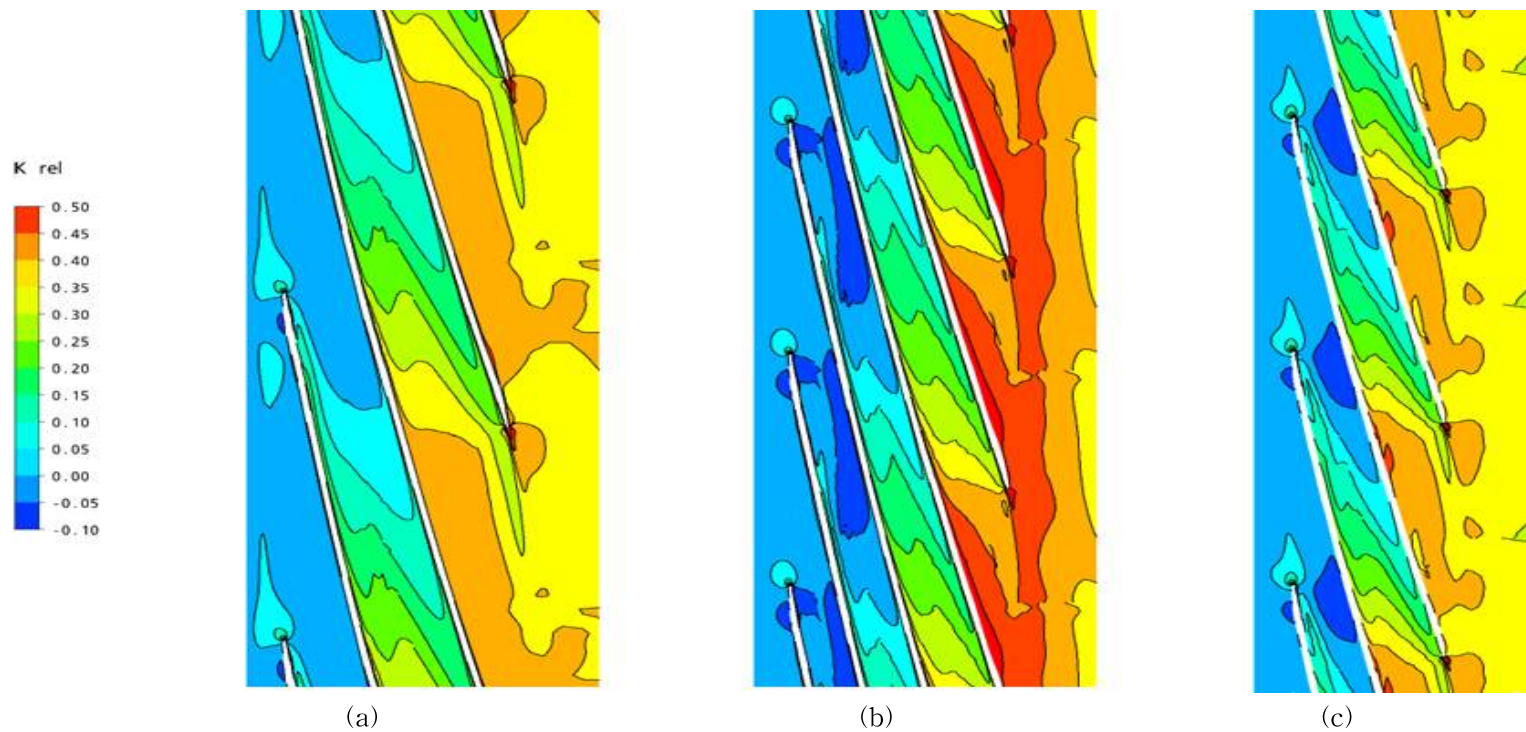


Fig. 3.19 Relative total pressure loss characteristic at 90 % span: (a) Z2s2; (b) Z3s3; (c) Z3s2

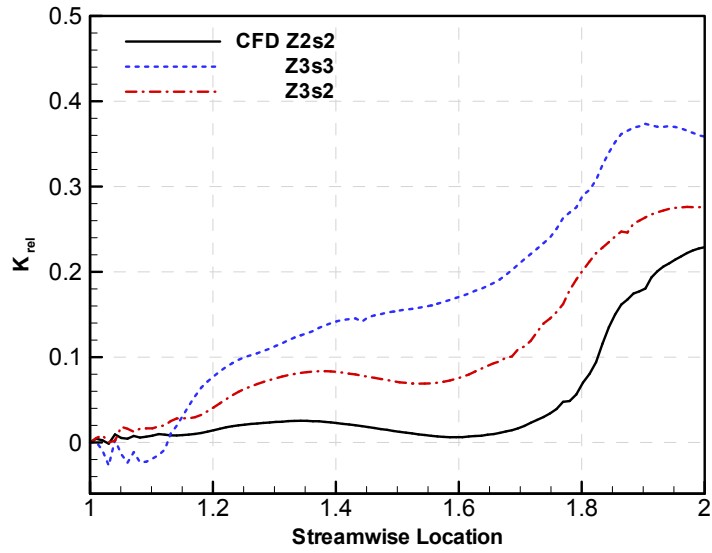


Fig. 3.20 Radial and tangential mass averaged relative total pressure loss coefficient at an inducer

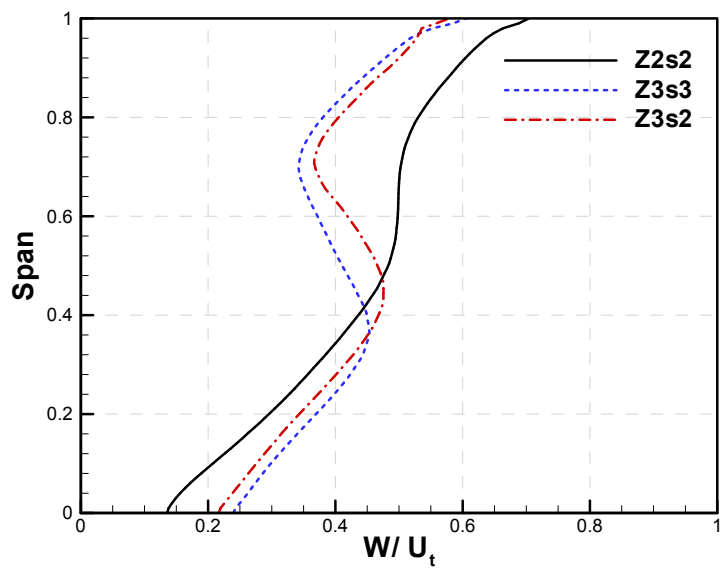


Fig. 3.21 Relative velocity distribution at an inducer outlet

Chapter 4. Empirical Equation

In this chapter, first, the purpose of the empirical equation is to analyze the principle for the deviation angle and the efficiency. Second one is to compare with the results applied the effect of the blade number and the solidity. Final is to recommend the new efficiency empirical equation.

At chapter 4.1, the deviation angle was mentioned. The efficiency empirical equation was covered in chapter 4.2.

4.1 Deviation angle

The flow leaving an inducer blade does not follow the blade camber line at the trailing edge. This deviation arises partly because the flow is diffusing within the blade passages. This means that the streamlines are diverging and therefore the flow is not moving in a single direction. This effect is exacerbated by the spacing of the blades because the flow is guided less by the blade when they are further apart. The deviation is further increased by viscous effects since any boundary layer growth on the blade surfaces will generate a blockage that modifies the effective blade shape.

Howel (1945) derived an empirical equation to relate the nominal deviation, δ^* occurring at the nominal incidence angle, i^* with blade

geometry:

$$\delta^* = m \theta \left(\frac{p}{l} \right)^n \quad (4.1)$$

$$\theta = \beta_2 - \beta_1 \quad (4.2)$$

$$m = 0.23 (2a/l)^2 + \beta_2^*/500 \quad (4.3)$$

where $n \approx 0.5$ for compressor cascades, $n \approx 1$ for compressor inlet guide vanes (these are actually turbine blades as they accelerate the flow), and a is the distance of the maximum blade camber from the leading edge. The value of m depends upon the shape of the camber line and the blade camber.

The deviation angles of the experiment test, the numerical calculation angle, and the result for using this empirical equation are shown in Table 4.1. As noted in Chapter 3, the trend of the deviation was changed through the inducer outlet. The position B about pressure rise characteristics was selected to the same condition for the experiment test. However, the deviation angle of the position A was used since the deviation angle be able to applied by the effect of the decreased diameter at position B. The deviation angle of the numerical calculation was directly obtained by the subtraction between the flow angle and the outlet blade angle, However, the deviation angle of the experiment test was obtained by the work coefficient because it was impossible to get flow angles.

Fig 4.1 shows the deviation angle distributions between the empirical equation and the numerical calculation at position A. According the empirical equation, the deviation angle is proportional to the pitch, but inversely proportional to the blade angle. Thus, the deviation angle of Z3s3 was smaller than that of Z2s2, and was larger than that of Z3s2. The deviation angle had a same value for an identical solidity, which means that the deviation angle did not applied by the blade number effect. However, the deviation angle of the numerical calculation was different. the deviation angle of Z3s2 was larger than that of Z2s2. It know that the deviation angle was applied by the blade number effect even the same solidity.

4.2 Efficiency

When designing the inducer, valuables or performances are predicted while each parameters are determined, and then these results are reflected. It is very effective and rational design method. Many empirical equations are used to predict the performance. Typical performances of the inducer outlet are the head and the efficiency. In Russia (2001), the mean line design method for inducer was developed as part of the high-pressure turbopump design. the empirical equation was suggested to use the efficiency prediction in this report.

$$\eta = 0.9 \tanh \left[\left(\frac{110}{\phi_{ind}^3} \right)^{0.55} \left\{ \frac{2}{\sqrt{s}} - 0.1 - 0.005(\beta_{b2} - \beta_{1b}) \right\} \right] \quad (4.4)$$

$$\phi_{ind} = 2.13 \frac{D_1}{\sqrt[3]{Q/w}} \quad (4.5)$$

$$D_1 = \sqrt{D_{1t}^2 - D_{1h}^2} \quad (4.6)$$

$$\eta = f \left(\phi, Re, s, \frac{p}{D} \dots \right) \quad (4.7)$$

$$\frac{p}{D} = \frac{\pi D}{Z} \frac{1}{D} \approx \frac{1}{Z} \quad (4.8)$$

In this chapter, the efficiency of the inducer was evaluated to compare with the empirical equation. Fig 4.2 shows the efficiency of the empirical equation and the experiment test. The efficiency of Z2s2 was the highest and then, the value of Z3s2 and Z3s3 were followed. In Z2s3 case, the efficiency of the experiment test was 10.1 % smaller than that of Z2s2 at design mass flow rate ($\phi = 0.101$). However, the efficiency of Z3s2 decreased by 4.81 % less than that of Z2s2. In empirical equation, the efficiency curve of Z3s3 was 14.69 % smaller than that of Z2s2 at design mass flow rate. According to the empirical equation, valuables of the efficiency are mass flow rate, rotating speed, size, solidity and blade angles except the blade number. So the efficiency of Z2s2 and Z3s2 had a same value because It seems that this empirical equation does not

reflect the blade number effect. Therefore, a new empirical equation included in the blade number effect is suggested. Two more models were added, since the new empirical equation based on three models were not sufficient to obtain the reliability.

Increasing the solidity with respect to the three bladed inducer, the fourth was selected for comparison model(Z3s4), and the four bladed inducer with the same solidity of the basic inducer was named the Z4s2. Fig 4.3 shows the shape of these model. The experiment test did not inevitably, so the numerical calculation was only carried out, and the results reflected to the new empirical equation. Fig 4.4 shows the pressure rise curves of the inducer for all cases. The pressure rise performance curves of Z3s4 and Z4s2 also had a same trend compared with others. The comparison of the efficiency curves was shown in Fig 4.5. As mentioned before, the efficiencies of Z2s2, Z3s2, and Z4s2 had a same result which not reflected in the blade number. The new efficiency empirical equation was suggested for using all five cases. The efficiencies of Z3s4 and Z4s2 were reflected by the correction between the numerical calculation and the experiment test. The term of blade number was considered based on the minimum blade number, and the coefficients were condignly modified by differences of the blade number and the solidity respectively. Fig 4.6 and Fig 4.7 show the graph to find the factor of the solidity and the blade number.

$$CF = \frac{\tanh^{-1}(\eta/0.9)}{\left(\frac{110}{\phi_{ind}^3}\right)^{0.55}} + 0.1 + 0.005(\beta_{b2} - \beta_{b1}) \quad (4.9)$$

A new empirical equation was defined as:

$$\eta = 0.9 \tanh \left[\left(\frac{110}{\phi_{ind}^3} \right)^{0.55} \left\{ \frac{2}{\sqrt{s}} - 0.184(Z-2) - 0.1 - 0.005(\beta_{2b} - \beta_{1b}) \right\} \right] \quad (4.10)$$

Fig 4.8 shows the efficiency comparison of the experiment test and the new empirical test. Although the results for a new empirical equation were not exactly same, it knows that the blade number effect considered the gap between both results was more smaller. So, from now on it is need the efforts to get the reliability for many other inducers.

Table 4.1 Deviation angle of Inducers.

Inducer		Blade angle	Deviation angle		
		All	Z2s2	Z3s3	Z3s2
EMP	Mid	16.3°	5.72°	4.46°	5.712°
EXP	Mid	16.3°	5.56°	5.62°	5.69°
CFD	Hub	31.2°	7.76°	11.69°	11.36°
	Mid	16.3°	9.31°	8.37°	10.51°
	Tip	10.91°	5.34°	4.74°	6.37°

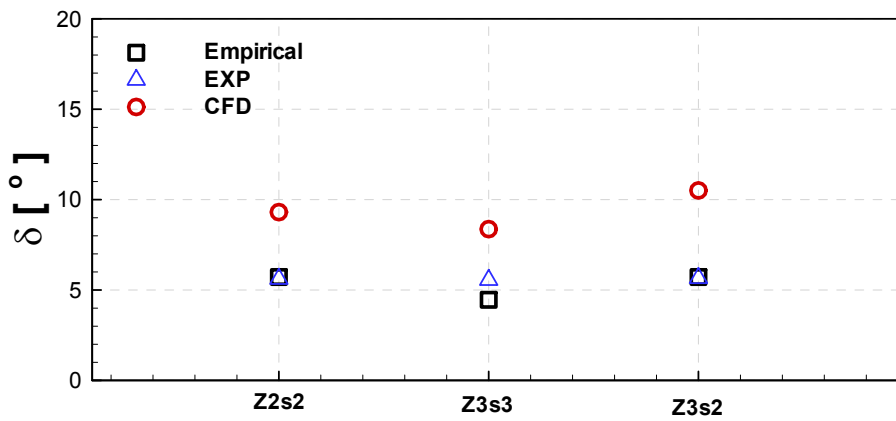


Fig. 4.1 Deviation angle distribution for an inducer

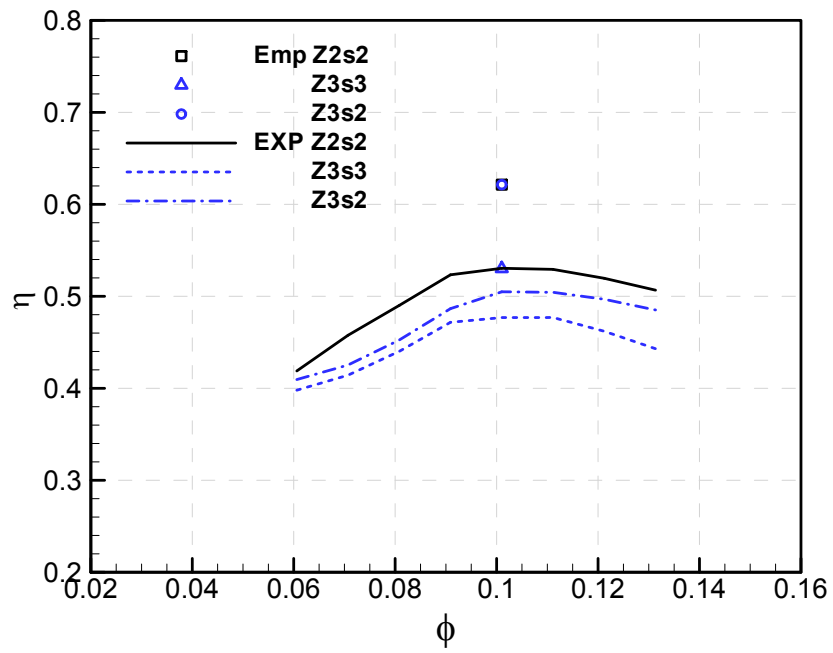


Fig. 4.2 Comparison of the efficiency empirical equation with the experiment test

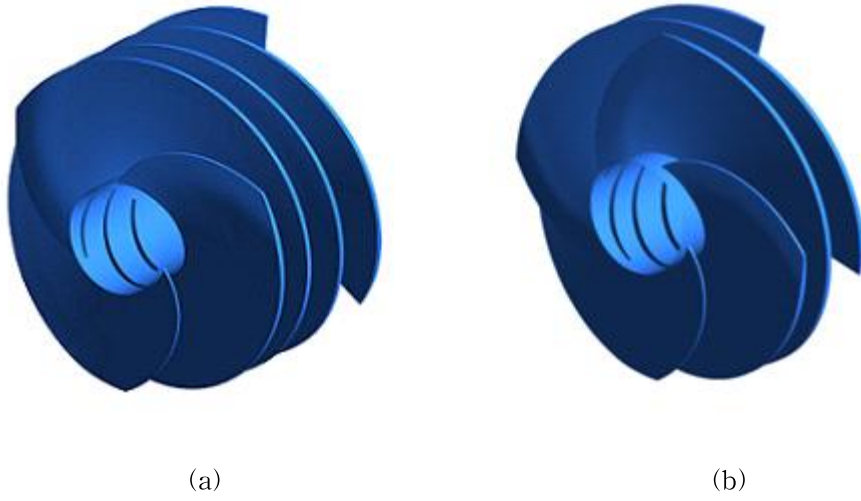


Fig. 4.3 Inducer Models: (a)Z3s4 ; (b)Z4s2

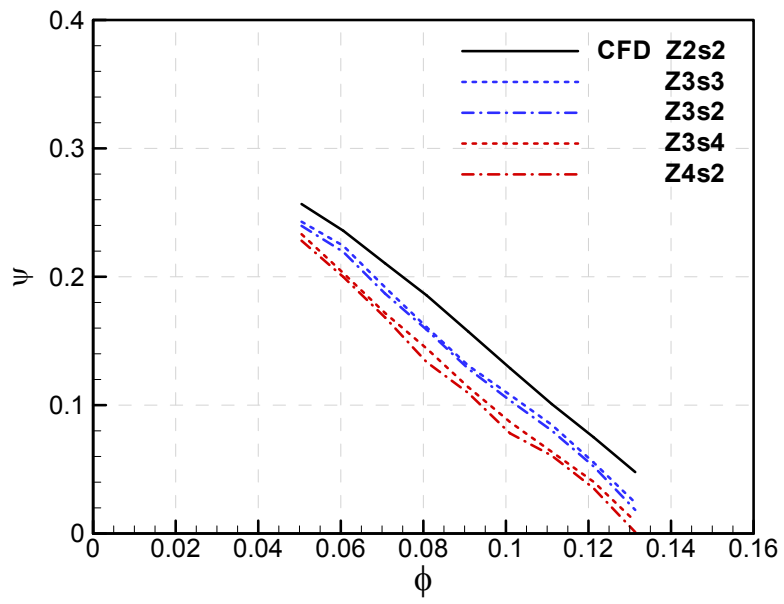


Fig. 4.4 Comparison of the pressure rise performance

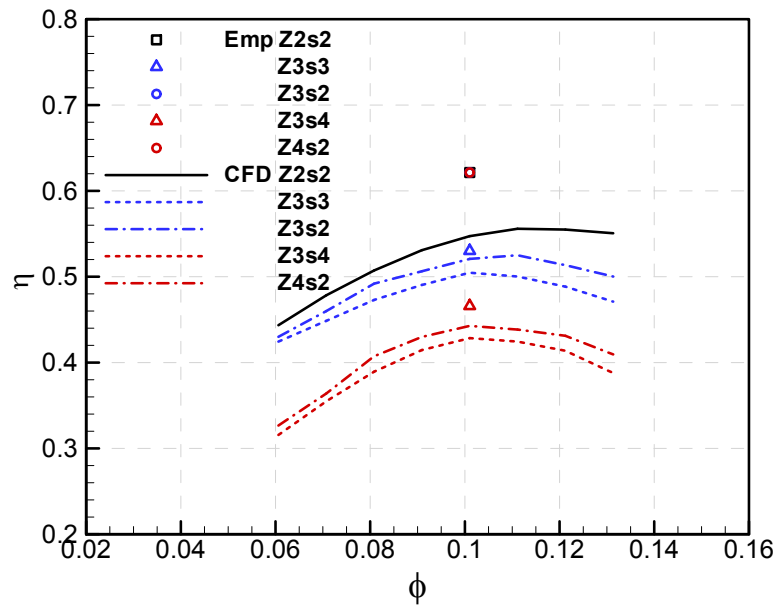


Fig. 4.5 Comparison of the efficiency empirical equation with the numerical calculation

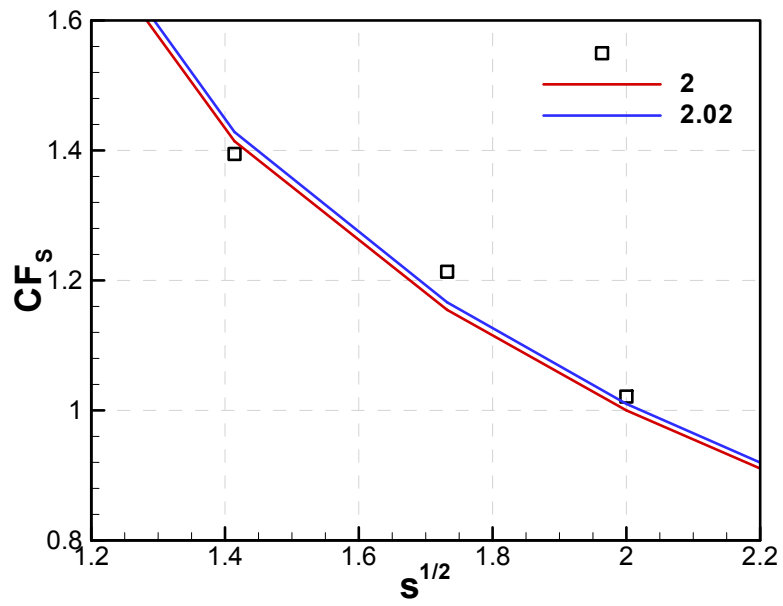
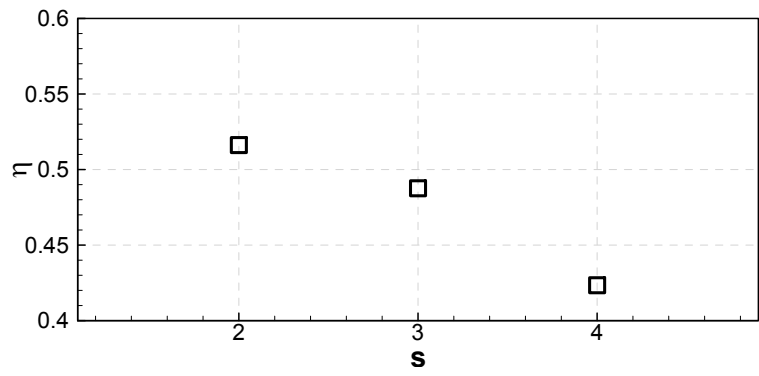


Fig. 4.6 Factor of the solidity

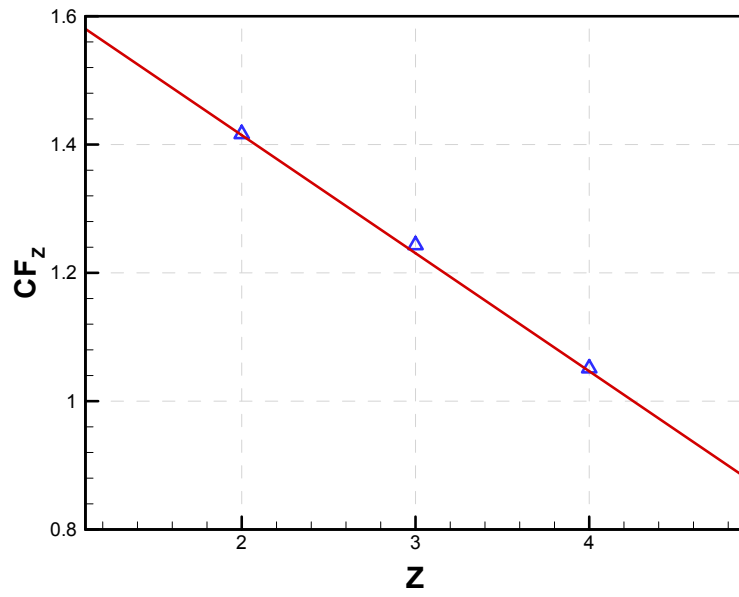
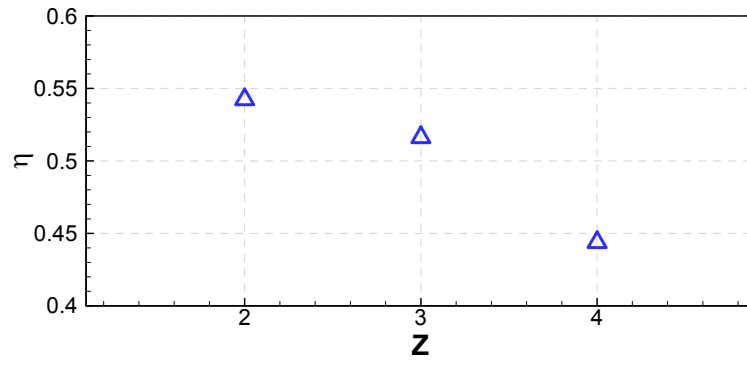


Fig. 4.7 Factor of the blade number

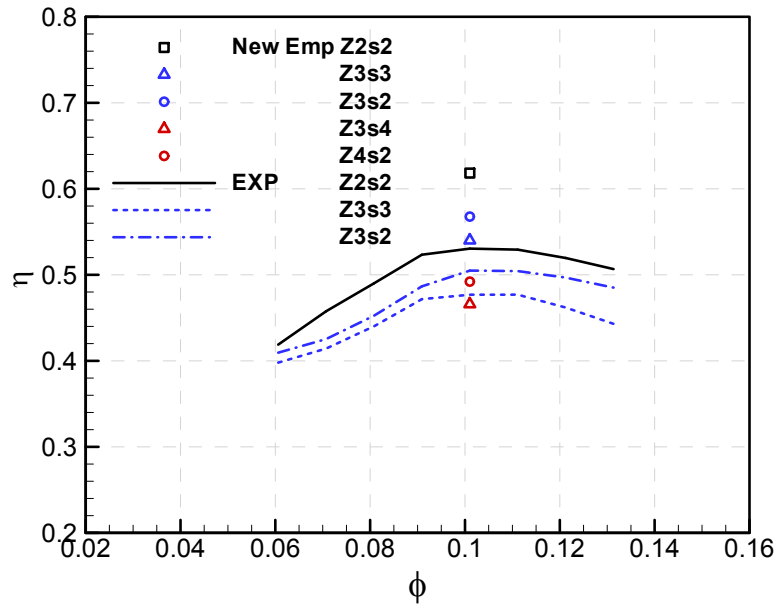


Fig. 4.8 Comparison of the new efficiency empirical equation with the experiment test

Chapter 5. Cavitation Instability

In this chapter, first, the purpose of cavitation phenomenon is to comprehend the principle of the cavitation. Second one is to investigate cavity characteristics related to the inception and the head drop and verify the empirical required $NPSH(3\%$ head drop pont). cavitation. Final is to analyze cavitation with the results applied the effect of the blade number and the solidity.

5.1 Fundamental of cavitation

Cavitation is the formation of bubbles filled with vapor or gas inside initially homogeneous liquids under very low pressure. It can be made by de-pressurization and differs from boiling where thermal energy drives the local temperature to exceed the saturation temperature as shown in Fig 5.1. Since a cavitation process is typically too rapid to assume thermal equilibrium at the interface, it is treated as a process at approximately constant temperature(practically isothermal). All liquids are susceptible to cavitation as soon as the local static pressure drops below a certain pressure value known as the vapor pressure which is a function of the surrounding liquid temperature. The bubbles collapse when they encounter higher pressure than the vapor pressure.

The tendency to cavitation is characterized by the cavitation number was defined as

$$\sigma = \frac{P_t - P_v}{\frac{1}{2}\rho U_t^2} \quad (5.1)$$

where the numerator represents the difference between reference pressure and vapor pressure, and the denominator represents the dynamic pressure. As cavitation number decreased, the tendency that cavitate the vapor increases.

Cavitation can be observed in a variety of engineering systems, such as venturi tubes, nozzles, injectors, pumps, marine propellers, hydro foils, and underwater bodies. Nowadays, cavitation can be detected easily due to miniaturization and speed-up of hydraulic machinery. Cavitating flows in hydraulic machines almost always cause unwanted phenomena: deteriorating the machine performance, imposing the additional forces on the solid structures, producing noise, generating vibration and even entire system oscillation, and enhancing wall erosion. If the damage is concentrated on some specific area, pieces of metal structures from the blade surface flake off due to fatigue failure. Due to undesirable effects induced by cavitation, researchers have been motivated to study in wide fields of cavitation such as bubble dynamics, instabilities, cavitation noise, cavitation erosion, cavitation luminescence, thermodynamic attenuation of cavitation and so on.

5.2 Various type of cavitation

As shown in Fig. 5.2, under the circumstance where the inducer is designed to have some magnitude of tip clearance, various types of cavitation occurring in the inducer can be classified: tip vortex cavitation, bubble cavitation, blade cavitation, backflow cavitation and tip leakage vortex cavitation, depending on how and where cavities are generated. However, the classification is somewhat ideal and arbitrary, and they can arise simultaneously with complex interaction, so to distinguish them is ambiguous.

When decreasing inlet pressure from cavitation-free condition, cavitation inception is almost always detected firstly as the tip vortex cavitation. Due to the tip interaction between the blade tip and the casing, tip vortex is generated and bubbles are trapped into the low pressure region in the vortex core.

Bubble cavitation usually forms on the suction surface of the blade. Nuclei (microbubbles or solid particles) in the inflow grow to observable size when they reach in the regions of low pressure, and then collapse when they are convected into regions of higher pressure. In most cases, it has little effect on the flow field. The inception, growth and collapse of bubble cavitation can be understood using Rayleigh-Plesset equation with some assumptions.

Blade cavitation is a type of cavitation in which cavity bubbles form generally on the suction surface of the blade and remain attached to the surface. It is also termed sheet cavitation in a hydrofoil or propeller

blade, attached cavitation in bluff bodies and blade cavitation in pumps. Below a certain length of the cavity, it acts like steady-state cavitation. However, when blade cavitation becomes larger than a certain extent, it encounters a strong re-entrant jet formed at the closure of the cavity and this jet is directed toward the leading edge. Then, the rear part of the cavitation sheet breaks off and transforms into a cloud cavitation, and subsequently, another cavity grows at the leading edge. Oscillation of the cavity length and unsteady behavior are observed. Unsteady characteristics of the blade cavitation have been extensively studied. Blade cavitation which closes and collapses on the suction surface of the blade is referred to as partial cavitation. At very low cavitation number, the cavity may extend downstream of the trailing edge of the blade. This long cavity is termed supercavitation. Supercavitation is used in high-speed propeller to greatly reduce the skin friction on the immersed body. Even at design operating condition, backflow occurs in the upstream annular region with a swirl velocity of about 20~30 % of the impeller tip velocity and axial upstream extent of many diameters of the inlet diameter. Backflow cavitation arises when the pressure at the core of a backflow vortex formed at the boundary between straight main flow and swirling backflow is lower than the vapor pressure.

Tip leakage vortex cavitation often occurs in the low pressure region of vortex developed as a result of the tip clearance between the blade tip and casing wall. Due to the pressure difference between pressure side and suction side of the blade, leakage flow is driven and tip leakage vortex by rolling up of the shear layer between main flow and tip

leakage flow is formed. Tip leakage flow entrains secondary flow, and cavitation associated with tip clearance which can manifestly distinguish the inducer with the tip clearance from the inducer without the tip clearance is established. In real inducers with tip clearance, a large amount of tip vortex cavitation, tip leakage vortex cavitation, blade cavitation, and backflow cavitation are generally found. However, only a few studies have focused on the understanding of basic characteristics of those kinds of cavitation instantaneously.

Rotating cavitation is a local cavitation instability in which the cavities propagate from blade to blade in much the same way as rotating stall. However, in the most typical mode, the cavitated region rotates slightly faster or slower than the inducer for rotating cavitation, while the stalled region in rotating stall rotates much slower than the rotating speed of the inducer. The rotating stall is characterized by several stall cells of velocity deficiency which rotate at 15 %~50 % speed of the rotor speed, thus accompanied by a drop in pressure rise and performance in off-design operating regime of low flow rate. But, rotating cavitation occurs even with negative slope of the static pressure performance curve. Besides conventional forward travelling mode with the frequency range of 1.1~1.5 fn. Backward travelling mode with the frequency range of about 0.9 fn was also identified. The occurrence of rotating cavitation has been extensively reported in the development of most high performance liquid propellant rocket fuel feed system, including the American Space Shuttle Main Engine, the European Ariane 5 engine, and the LE-7 of the H-II and H-IIA rockets in Japan. There

are two type of the cavitation, namely, 'super/sub-synchronous' and 'synchronous' rotating cavitation. Synchronous rotating cavitation is known as asymmetric cavitation, one of several sources of cavitation causing shaft vibration. It is steady and asymmetric phenomenon in which unevenness of the cavity does not propagate. Synchronous rotating cavitation also results in severe synchronous shaft vibration and causes degradation of suction performance due to an asymmetric cavity pattern. This phenomenon is commonly observed in three-bladed inducers.

Asymmetric cavitation with uneven cavities on each blade (Tsujiimoto, 1997) is another type of cavitation instabilities often observed; This phenomenon was observed in the first test of the LE-7A engine for H-II A rocket. (Fujii, 2003) It causes a large amplitude synchronous shaft vibration, since the mean blade stress near the leading edge are significantly different from those located blades because of the asymmetry of the cavities on each blade. But, the fluctuation of the stresses on each blade is low since the flow viewed in rotating frame is relatively steady, showing different characteristics from rotating cavitation.

Cavitation surge is a system instability in which the flow rate of the hydraulic system fluctuates with in-phase cavity volume fluctuation on each blade. It is a viciously unstable phenomenon, in which all blade cavities in the inducer become periodically elongated and shortened with the same phase and the flow rate is changed. The surge is essentially one-dimensional axisymmetric flow oscillation accompanied by a large

fluctuation in pressure rise leading to mechanical damage through vibration and excessive temperature. It is known that cavitation surge to occur more readily when the inducer is more heavily loaded; in other words, at lower flow coefficients than higher one when backflow also occurs.

5.3 Cavitation model

Since 1980s, numerical simulations have been started to understand the characteristics and mechanism of complex cavitating flows with phase change, vortex shedding, turbulence, unsteady behavior, bubble collision and collapse aided by rapidly advanced computing capability. However, the remaining difficulty is that governing equations to describe the cavitating flows accurately and physical model for interaction between each phase are not established, yet. At present, some physical models for cavitating flows are proposed, and they can be divided roughly into three-categories: one-phase one-fluid analysis where only liquid phase outside cavity is solved and the transfer of the liquid-vapor interface is captured, two-phase two-fluid analysis where both liquid phase outside the cavity and gas phase inside the cavity individually are solved, and two-phase one-fluid analysis where liquid and gas phases inside and outside the cavity are treated as a locally homogeneous mixture.

In ANSYS CFX, in the context of two-phase one-fluid analysis,

cavitating flows are analyzed as a homogeneous mixture. The Rayleigh-Plesset model based on the rate equation controlling vapor generation and condensation is adapted as an interphase mass transfer model. Since it has governing equations for one mixture, computation time is reduced drastically. Due to such merits, ANSYS CFX is getting used widely in industry and proved to be able to predict the cavitation phenomena with reasonable accuracy. The governing equations describing the cavitation process assume a two-phase one fluid three-component system, with no consideration of slip velocity between phases and thermal effect. Three components are: liquid(primary phase), vapor (primary phase), and non-condensable gas(dispersed phase).

Their relative quantity is expressed by a volume fraction, α . The sum of all volume fractions must be unity

$$\alpha_l + \alpha_v + \alpha_d = 1 \quad (5.2)$$

Similarly, mass fraction, y can be described:

$$y_l + y_v + y_d = 1 \quad (5.3)$$

where $y_l = \alpha_l \rho_l / \rho$, $y_v = \alpha_v \rho_v / \rho$, and $y_d = \alpha_d \rho_d / \rho$

In general, non-condensable gas can be assumed to be dispersed and well-mixed in liquid phase with a constant mass fraction, y_d . On this basis, volume fraction α_m is introduced where $\alpha_m = \alpha_l + \alpha_d$. The density associated with the primary liquid phase with non-condensable gas becomes:

$$\rho_m = \frac{1}{(1-y_d)/\rho_l + y_d/\rho_d} \quad (5.4)$$

and governing volume fraction equation for α_m becomes:

$$\frac{\partial}{\partial t}(\rho_m \alpha_m) + \frac{\partial}{\partial x_j}(\rho_m u_j \alpha_m) = \dot{S}_l \quad (5.5)$$

where \dot{S}_l and \dot{S}_v represent the source terms which account for the destruction and generation (condensation and evaporation) of the vapor bubbles, respectively and $\dot{S}_v = -\dot{S}_l$.

In two-phase one-fluid model, it is assumed that all phases share the same velocity, thus the governing equations of the mixture for mass and momentum are:

$$\frac{\partial \rho}{\partial t} + \frac{\partial}{\partial x_j}(\rho u_j) = 0 \quad (5.6)$$

$$\frac{\partial \rho u_j}{\partial t} + \frac{\partial}{\partial x_j}(\rho u_j u_i) = \frac{\partial \tau_{ij}}{\partial x_j} - \frac{\partial P}{\partial x_i} \quad (5.7)$$

where the mixture density $\rho = \alpha_m \rho_m + \alpha_v \rho_v$, the velocity field u_j , and the stress tensor τ_{ij}

To take the dynamics of cavitation bubble into account and provide the rate equation governing vapor generation and condensation, simplified Rayleigh-Plesset equation is employed. For a single vapor bubble surrounded by liquid, the dynamic growth of the bubble can be described by the Rayleigh-Plesset equation:

$$R_B \frac{d^2 R_B}{dt^2} + \frac{3}{2} \left(\frac{dR_B}{dt} \right)^2 + \frac{2\sigma}{\rho_l R_B} = \frac{P_v - P}{\rho_l} \quad (5.8)$$

where R_B represents the bubble radius, P_v is the pressure in the bubble (assumed to be the vapor pressure at the liquid temperature), P is the pressure in the liquid surrounding the bubble, σ is the surface tension coefficient between the liquid and vapor. Note that this is derived from a mechanical balance, assuming no thermal barriers to bubble growth. Neglecting the second order terms (which is appropriate for low oscillation frequencies) and the surface tension, this equation reduces to:

$$\frac{dR_B}{dt} = \sqrt{\frac{3}{2} \frac{P_v - P}{\rho_l}} \quad (5.9)$$

The rate of change of bubble volume follows as:

$$\frac{dV_B}{dt} = \frac{d}{dt} \left(\frac{4}{3} \pi R_B^3 \right) = 4\pi R_B^2 \rho_v \sqrt{\frac{3}{2} \frac{P_v - P}{\rho_l}} \quad (5.10)$$

and the rate of change of bubble mass is:

$$\frac{dm_B}{dt} = \rho_v \frac{dV_B}{dt} = 4\pi R_B^2 \rho_v \sqrt{\frac{3}{2} \frac{P_v - P}{\rho_l}} \quad (5.11)$$

If there are N_B bubbles per unit volume, the volume fraction r_g may be expressed as:

$$r_g = V_B N_B = \frac{4}{3} \pi R_B^3 N_B \quad (5.12)$$

and the total interphase mass transfer rate per unit volume is:

$$\dot{m}_{fg} = N_B \frac{dm_B}{dt} = \frac{3r_g \rho_v}{R_B} \sqrt{\frac{2}{3} \frac{P_v - P}{\rho_l}} \quad (5.13)$$

For evaporation

$$\dot{m}_e = C_e \frac{3r_g \rho_v}{R_B} \sqrt{\frac{2}{3} \frac{P_v - P}{\rho_l}} \quad (5.14)$$

For Condensation

$$\dot{m}_c = C_c \frac{3r_g \rho_v}{R_B} \sqrt{\frac{2}{3} \frac{P - P_v}{\rho_l}} \quad (5.15)$$

To obtain an interphase mass transfer rate, further assumptions regarding the bubble concentration and radius are required. The Rayleigh Plesset cavitation model implemented in ANSYS CFX uses the following defaults for the model parameters:

$$R_B = 1 \mu m \quad (5.16)$$

$$C_e = 50 \quad (5.17)$$

$$C_c = 0.01 \quad (5.18)$$

5.4 Required NPSH

The net positive suction head(*NPSH*), which is the head required at the turbopump inlet to keep the liquid from cavitating or boiling. The turbopump inlet or suction surface is the low pressure point where cavitation will first occur. The *NPSH* is defined as

$$NPSH = \frac{P_t - P_v}{\frac{1}{2} \rho U_t^2} \quad (5.19)$$

Fig 5.3 is a graph of the head coefficient against cavitation number. Frequently, of course, both performance curves are presented dimensionally; then, for example, the *NPSH* is often used instead of the cavitation number as the abscissa for the cavitation performance graph. It is valuable to identify three special cavitation numbers in the cavitation performance graph. Consider a pump operating at a particular flow rate or flow coefficient, while the inlet pressure, *NPSH*, or cavitation number is gradually reduced. The first critical cavitation number to be reached is that at which cavitation first appears; this is called the cavitation inception number, σ_i . Often the occurrence of cavitation is detected by the typical crackling sound that it makes. As the pressure is further reduced, the extent (and noise) of cavitation will increase. However, it typically requires a further, substantial decrease in σ before any degradation in performance is encountered. When this

occurs, the cavitation number at which it happens is often defined by a certain percentage loss in the head rise, H , or head coefficient, as shown in Fig 5.3. Typically a critical cavitation number, σ_{cr} , is defined at which the head drop is 2, 3 or 5 %. The a critical $NPSH$ usually calls the required $NPSH(NPSH_r)$. In this study, the required $NPSH$ was defined at which 3 % head drop point. Further reduction in the cavitation number will lead to major deterioration in the performance; the cavitation number at which this occurs is termed the breakdown cavitation number, and is denoted by σ_b .

Figure 5.4 shows the suction performance curve of the inducer used for this study at design mass flow rate. The $NPSH_r$ of Z3s3 and Z3s2 increased 25.8% and 14.1%, respectively. A cavitation number that corresponds to the same $NPSH_r$ was shown Table 5.1. A notable point is that the suction performance curve of Z3s3 was gradually dropped until the collapse of head(Breakdown point) unlike other cases. The reason about this phenomenon is unclear up to now.

An empirical approach exists for describing the various effects of acceleration, which is essential for one-dimensional or preliminary performance modeling.

$$P = P_v = P_t - \lambda_b \left(\frac{1}{2} W_t^2 \right) \quad (5.20)$$

$$NPSH_r = \frac{C_{m,tip}^2 + \lambda_b W_{m,tip}^2}{2g} \quad (5.21)$$

Where λ_b is the blade cavitation coefficient and represents the

fraction of inlet kinetic energy which is involved in the local flow acceleration (static pressure reduction). At cavitation, λ_b was defined as:

$$\begin{aligned}
 0.2 \leq \lambda_b \leq 0.4 & \quad \text{Dixon (1978)} \\
 0.1 \leq \lambda_b \leq 1.0 & \quad \text{Practice} \\
 \lambda_b \leq 0.1 & \quad \text{Rocket turbopumps}
 \end{aligned}
 \tag{5.22}$$

Brozobsky(1989) expressed the blade cavitation coefficient more detailed

$$\lambda_b = a_o + b_o \phi \quad b_o = 0.115 \tag{5.23}$$

$$\begin{aligned}
 a_o = 0.043 \left(\sqrt[4]{\frac{\gamma}{i} - 1} \right) + 0.21 \sqrt{t/D} \\
 + \frac{0.11}{\sqrt[6]{L/D}} + 0.0027(Z-2) - 0.095
 \end{aligned}
 \tag{5.24}$$

Where γ is the wedge angle of the blade, t is the blade thickness. Usually, these geometrical parameters have general ranges.

$$\begin{aligned}
 0.8 \leq \gamma/i \leq 1.5 \\
 0.005 \leq t/D \leq 0.0045 \\
 L/D \geq 0.23 \\
 0.02 \leq a_o \leq 0.04
 \end{aligned}
 \tag{5.25}$$

Figure 5.5 shows the *NPSHr* performance curves of the empirical equation, the experiment test, and the numerical calculation. The biggest cause for the difference occurring between the experiment test and the numerical calculation is the cavitation model. As mentioned earlier, the

simplified Rayleigh Plesset model for the convenience numerical calculation was ignored the effect of a surface tension and linearized the term of the non-linearization. So the numerical calculation result did not exactly reflect the actual model for cavitation phenomenon. The empirical equation of $NPSHr$ was included with valuables of the blade number and the solidity. However, the result was significantly different. As the mass flow rate increased, but the lifting trend was the same compared to the experiment test.

5.5 Cavitation inception

In order to examine the characteristics of the cavitation inception, there inducers that used in this study were investigated. In general, as the inlet pressure decreased from non cavitation condition, cavitation occurred at blade tip called the tip vortex cavitation. And then, the tip vortex cavitation was getting longer and connected to generate the bubble cavitation increasingly. Fig 5.6 shows the visualization of the cavitation inception. It can be seen that both cavities occurred in these inducers. The cavitation number of inception is shown in Fig 5.8. As the number of blade increased, the cavitation inception also increased. However, the solidity effect did not changed to the inception. It knows that the cavitation inception is a feature unique to the leading edge of the tip locally. The static pressure was also have a similar decrease like the cavitation inception trend at the leading edge of the inducer in Fig

5.7. As the inlet pressure decreased further, the cavity became large and extended. To find the characteristics of the moment that the head was about to drop, three cavitation numbers ($\sigma = 0.059, 0.054,$ and $0.052,$ Fig 5.9) were selected, and compared with Z3s3 and Z3s2. Fig 5.10 shows the static pressure recovery coefficient curves. The static pressure recovery coefficient(C_p) is defined as

$$C_p = \frac{p - p_{in}}{\frac{1}{2} \rho U_t^2} \quad (5.26)$$

The static pressure recovery coefficients of Z3s2 were no different depend on the cavitation number. However, the pressure coefficients of Z3s3 were changed on the pressure surface(PS) and the suction surface (SS). To find the reason, the cavity shape was analyzed by a numerical calculation. Fig 5.11 shows the shape of the cavity at the tip of the blade leading edge. Since the inducer that used in this study was required to a high suction performance, the specific speed is low. So the incidence angle of the tip had the negative value. It can be seen that the tip vortex cavitation occurred on the suction surface although the size was not large. In Z3s3 case, the cavity occurred on the suction surface under $\sigma=0.054,$ and the cavity abruptly generated under $\sigma=0.052,$ which in on the pressure surface. This cavity affected the next blade that located on the suction surface. As a result, the pressure of the fluid coming to the leading edge reduced due to the interference with the next blade.

Because of this, the head drop started once the cavity occurred on the suction surface. If the cavitation inception staves off generation, the head drop is able to delay itself.

5.6 Effects of blade number and solidity

Fig 5.12~Fig 5.14 show visualizations of cavitation shape for the three cases at the design flow rate. Three cases had same characteristics of the inception, head drop point, critical $NPSH$, and breakdown except by the cavitation number. The main reason why the $NPSH_r$ was different between Z2s2 and Z3s2(Blade number effect) was the interference of the blade. As the blade number increases, the pitch is narrow, which means that the flow loss is not only big, the velocity at the inducer inlet is but also fast. Therefore, cavitation occurred under the earlier cavitation number. As mentioned earlier in Chapter 5.5, the difference of the head drop point was investigated for the solidity effect. Phenomena after head drop point to breakdown were just delayed. The camber may be one cause. Fig 5.15 is the schematic of the inducer blade. If the blade has not a camber, the pitch and the width were identical even the solidity was different. However, the shape of the blade that has a camber was changed depended on the solidity. Despite the same pitch, the width is narrow for Z3s3. From this cause, the velocity of Z3s3 was faster that of Z3s2, and the cavitation generated earlier. It seems that all of the cascade shape were determined after one blade

was designed, so the actual three dimensional blade shape was slightly different. Fig 5.16 shows the blade shape of the inducer, and Fig 5.17 is the graph of the blade angle from leading edge to trailing edge.

Flow instabilities were investigated by FFT analysis of the signals coming from the pressure transducers installed in the inducer casing wall and cavitation visualization. Fig 5.18 shows FFT analysis of cavitation for three cases at the design flow rate. It was known that the blade passing frequency(BPF) basically differs depending on the blade number(N2s2 vs N3s3, N3s2). As the inlet pressure decreases, a symmetry cavitation corresponding to 2 or 3 times the rotational speed appeared(a). An asymmetry cavitation corresponding to the rotational speed also occurred. Cavitation surge occurred at low frequency when the inlet pressure decreases further(b). In Z3s3 and Z3s2, rotating cavitation was strongly observed(c). On the other hand, rotating cavitation did not strongly occur in Z2s2 case. In Z3s2 case, it was found that the intensity of symmetry cavitation and rotating cavitation significantly weak compared with Z3s2. Cavitation surge, on the other hand, dramatically occurred. Especially, higher order rotating cavitation did not occur(d).

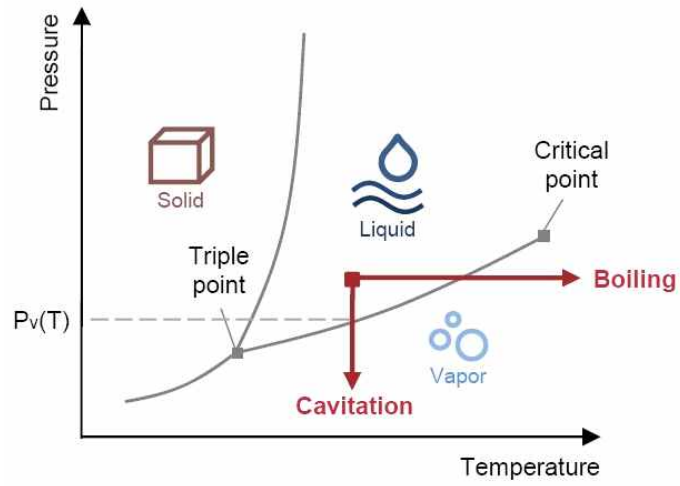


Fig. 5.1 Phase diagram of the water

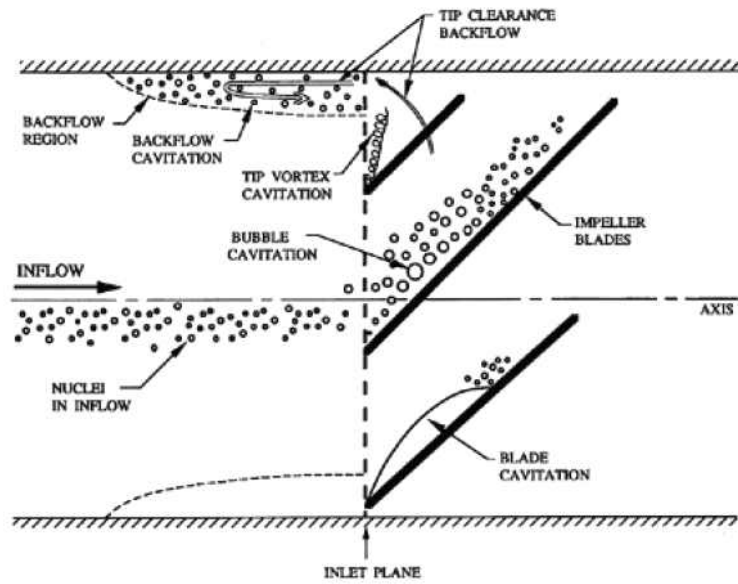


Fig. 5.2 Type of the cavitation

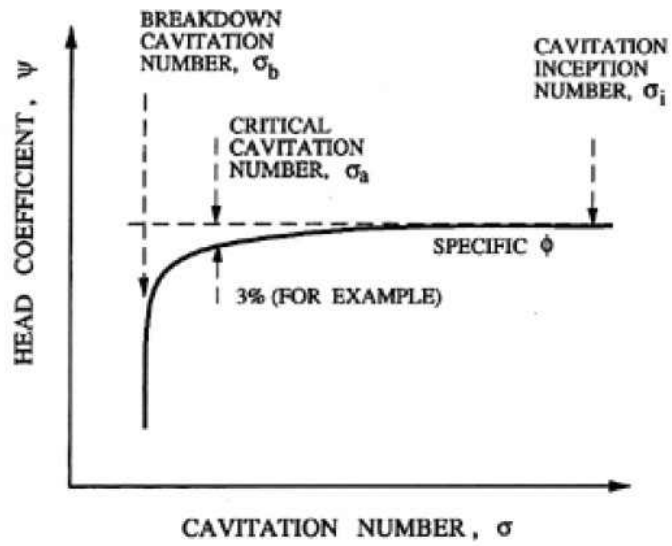


Fig. 5.3 Schematic of cavitation performance showing the three key cavitation numbers.

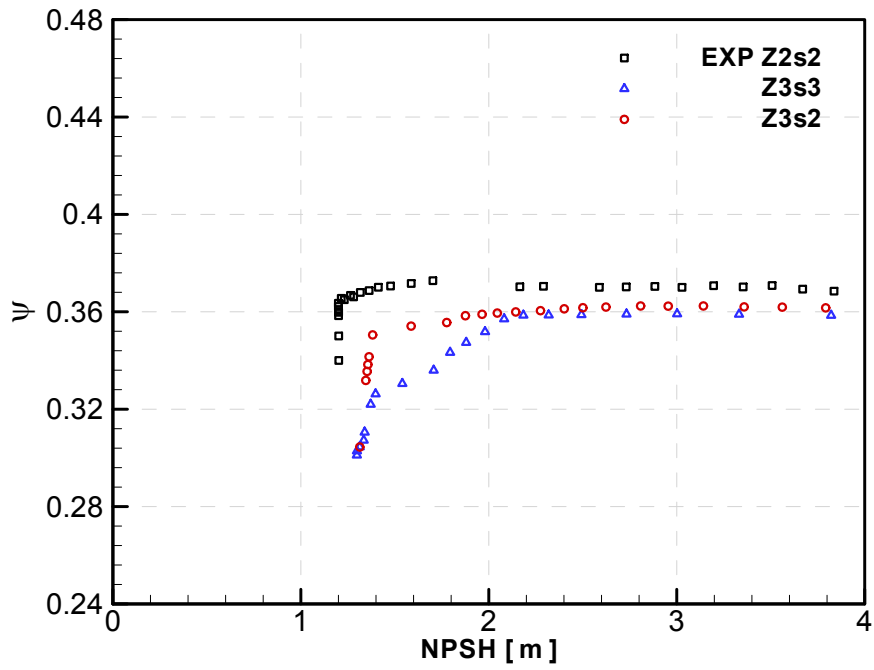


Fig. 5.4 Suction performance in the experiment test at design mass flow rate ($\phi = 0.101$)

Table 5.1 Required *NPSH_r* and the critical cavitation number

1.0 Q_d	<i>NPSH_r</i>	Cavitation Number
Z2s2	1.20 m	0.070
Z3s3	1.51 m	0.088
Z3s2	1.37 m	0.081

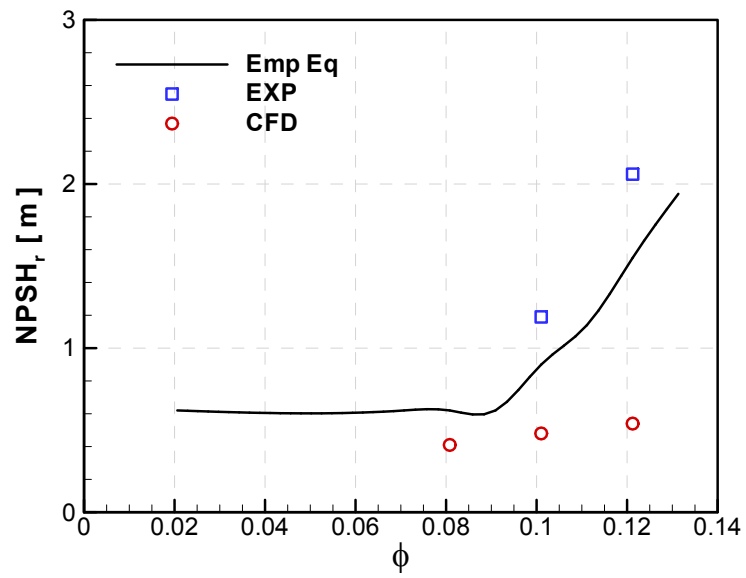


Fig. 5.5 Comparison of the suction performance

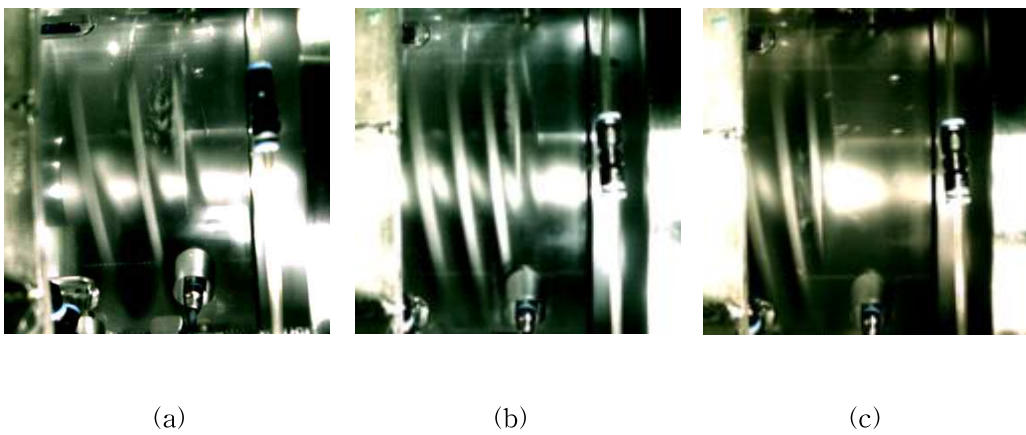


Fig. 5.6 Visualization of the cavitation inception: (a) Z2s2; (b) Z3s3; (c) Z3s2

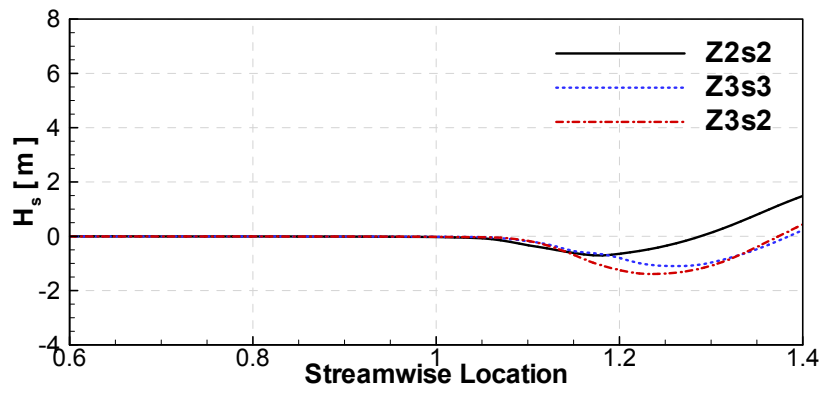


Fig. 5.7 Static pressure distributions at leading edge

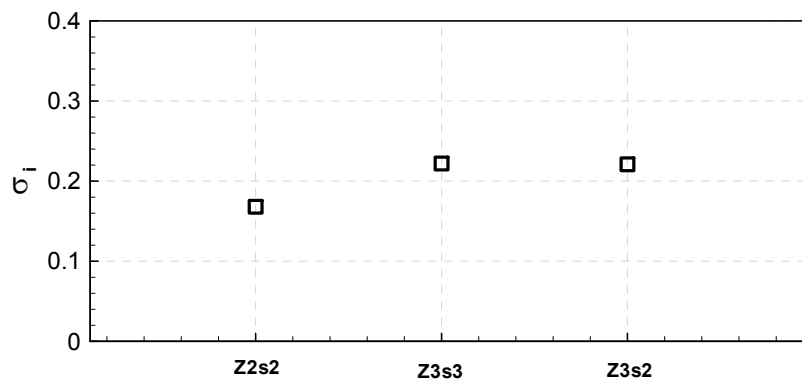


Fig. 5.8 Comparison of the cavitation inception

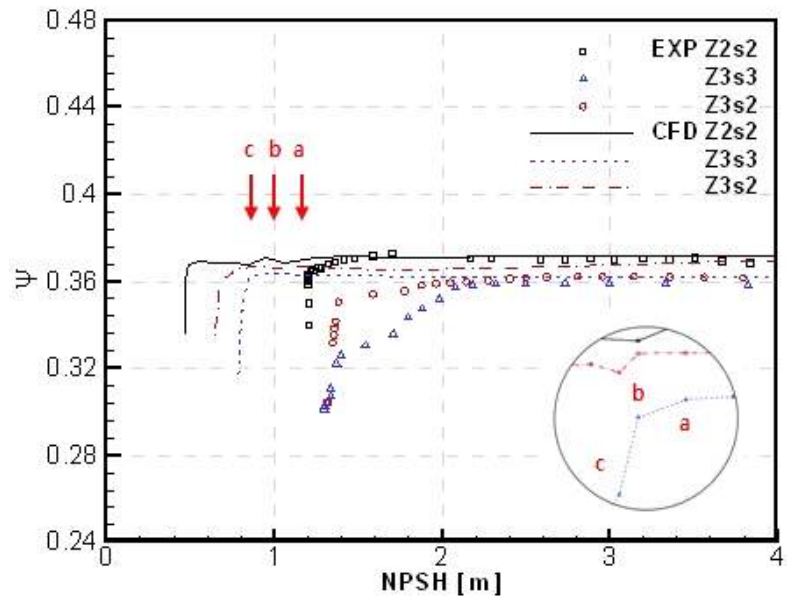
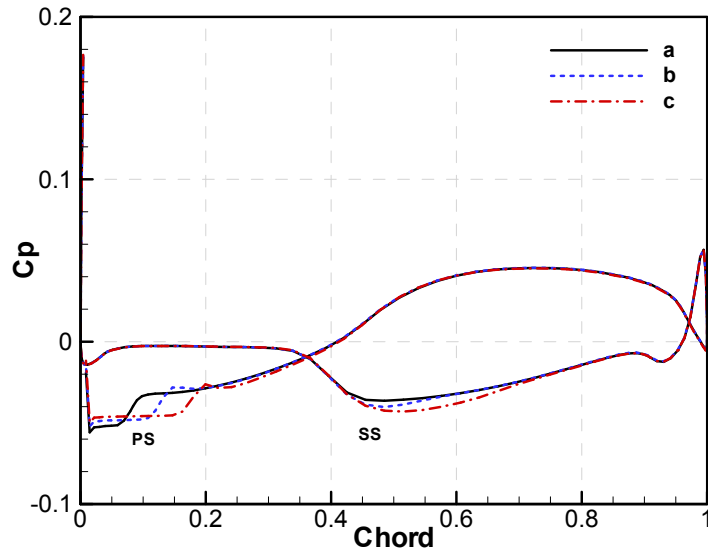
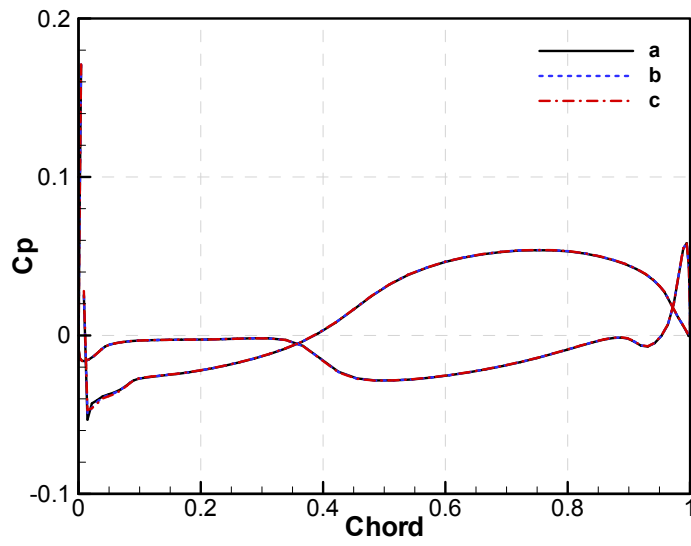


Fig. 5.9 Head drop point for the numerical calculation



(a)



(b)

Fig. 5.10 Static pressure recovery coefficient: (a) Z3s3; (b) Z3s2

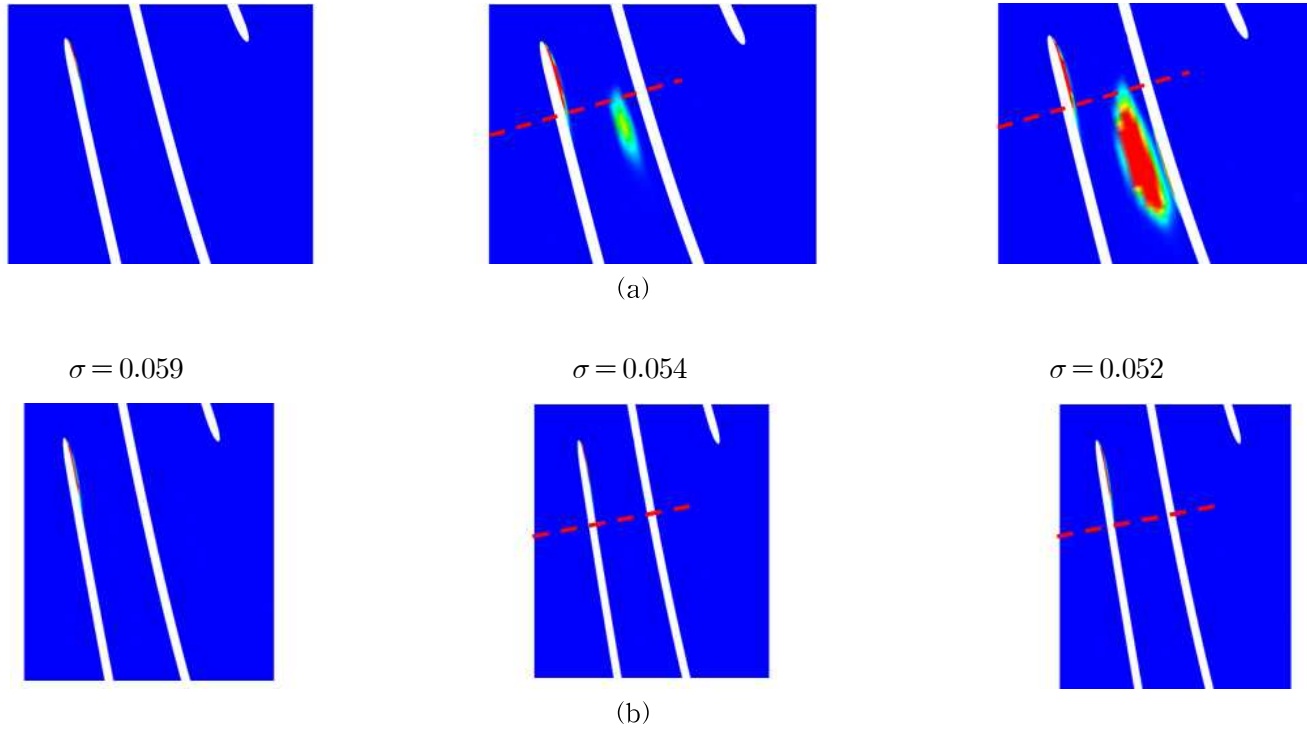


Fig. 5.11 Shape of the cavity: (a) Z3s3; (b) Z3s2



(a) $\sigma = 0.176$



(b) $\sigma = 0.151$



(c) $\sigma = 0.126$



(d) $\sigma = 0.086$

Fig. 5.12 Visualization of cavitation in Z2s2



(a) $\sigma = 0.194$



(b) $\sigma = 0.175$



(c) $\sigma = 0.145$



(d) $\sigma = 0.114$

Fig. 5.13 Visualization of cavitation in Z3s3



(a) $\sigma = 0.195$



(b) $\sigma = 0.153$

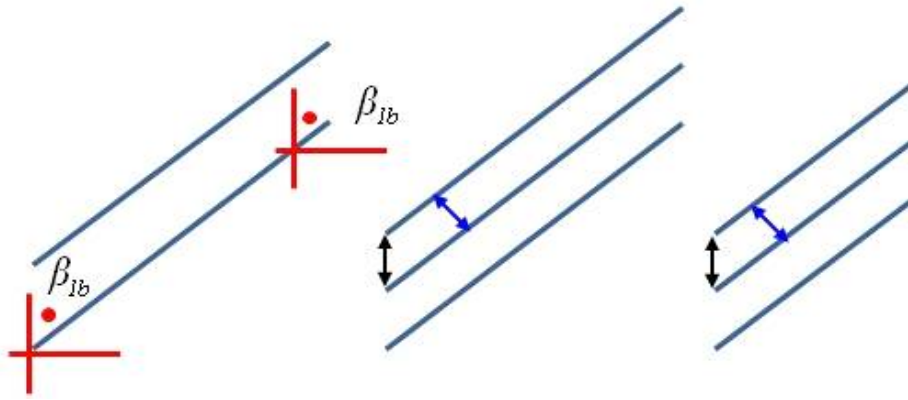


(c) $\sigma = 0.132$

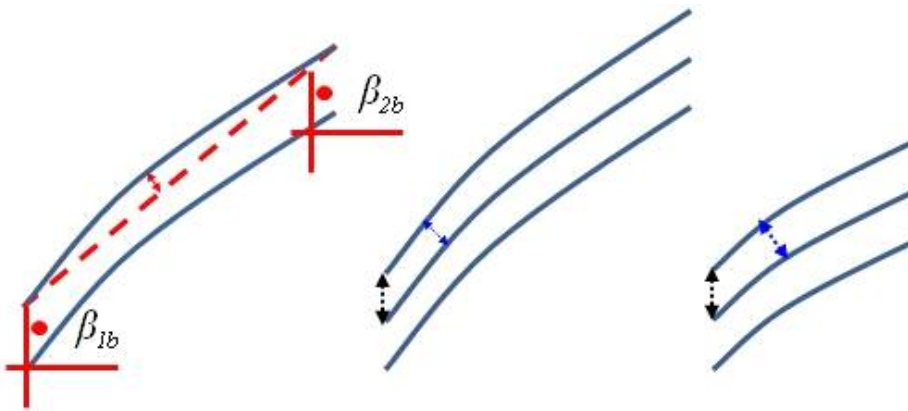


(d) $\sigma = 0.109$

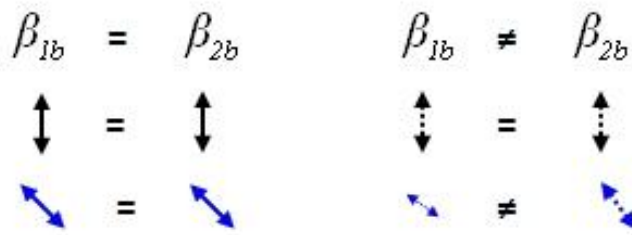
Fig. 5.14 Visualization of cavitation in Z3s2



(a) w/o camber



(b) w/ camber



(c)

Fig. 5.15 Schematic of the inducer blade

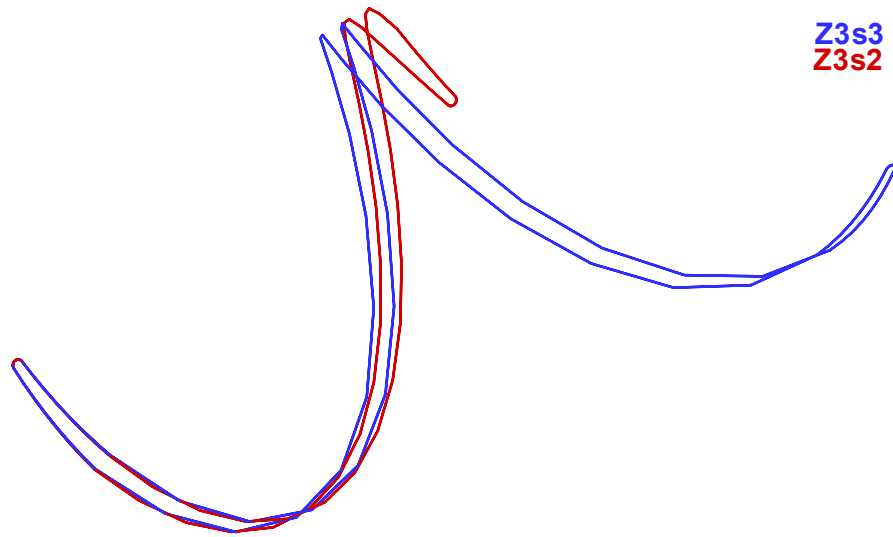


Fig. 5.16 Blade shape of the inducer

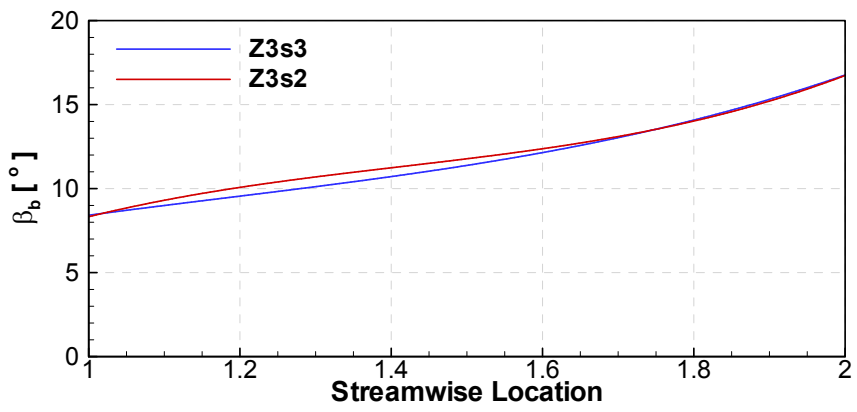
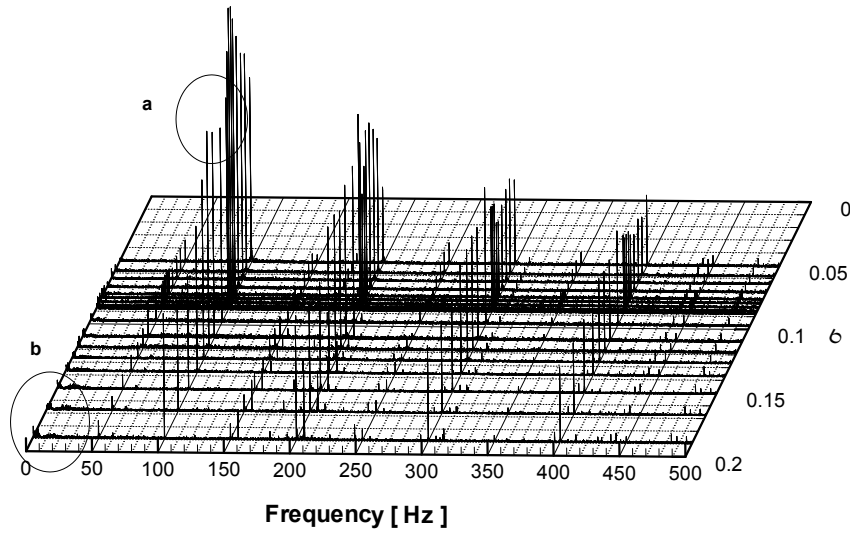
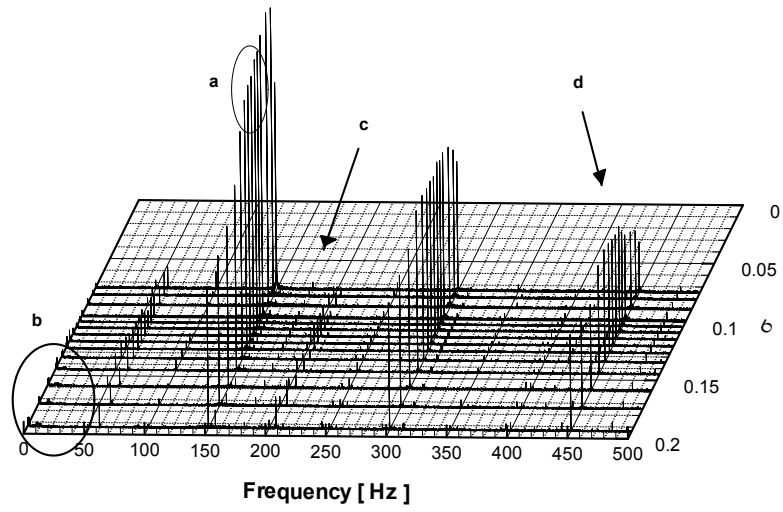


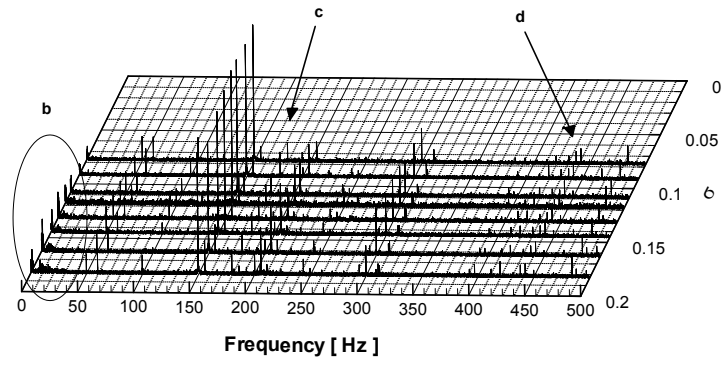
Fig. 5.17 Comparison of the blade angle



(a)



(b)



(c)

Fig. 5.18 FFT analysis of cavitation instabilities: (a) Z2s2; (b) Z3s3; (c) Z3s2

Chapter 6. Conclusions

6.1 Conclusions

This study presented the effect of the blade number and the solidity of a turbopump inducer. Before investigating the effect, the reason why two variables were selected for this study was examined. The experiment test and the numerical calculation were carried out for three inducers. and then, the results were analyzed. The results can be summarized as follows:

- (1) The total pressure rise of Z3s3 of the experiment test was 12.75 % smaller than that of Z2s2 at design mass flow rate, and the total pressure rise of Z3s2 decreased by 18.74 % less than that of Z2s2. The efficiency of Z2s2 was the highest and then, the value of Z3s2 and Z3s3 were followed.
- (2) The mass averaged deviation angle of Z3s2 was smaller than that of Z2s2 which represents comparison of the blade number effect. The mass averaged deviation angle of Z3s2 was larger than that of Z3s3. These trends were satisfied by the empirical rule.
- (3) The relative total pressure loss for all three cases increased.

Especially, the losses of Z3s3 and Z3s2 were bigger than that of Z2s2 and continued to the impeller inlet. Those loss characteristics influenced on the efficiency. Therefore, the efficiency of Z3s3 was the lowest compared with other cases, even though the pressure rise performance of Z3s3 was higher than that of Z3s2.

- (4) The existing efficiency empirical equation did not reflect to the blade number. So the new empirical equation was suggested by applying the blade number effect. To get the reliability, two more models were added. The efficiencies of the Z3s4 and Z4s2 were reflected the correlation between the numerical calculation and the experiment test.
- (5) The suction performance curve of the inducer used for this study at design mass flow rate. The $NPSHr$ of Z3s3 and Z3s2 increased 25.8% and 14.1%, respectively. The biggest cause for the difference occurring between the experiment test and the numerical calculation is the cavitation model. The empirical equation of $NPSHr$ was included with valuables of the blade number and the solidity. However, the result was significantly different.
- (6) As the inlet pressure decreased from non cavitation condition, cavitation occurred at blade tip called the tip vortex cavitation. And then, the tip vortex cavitation was getting longer connected to generate the bubble cavitation increasingly. Cavitation inception was not related to the solidity, and only depended on the blade number.

- (7) The pressure of the fluid coming to the leading edge reduced due to the interference with the next blade. Because of this, the head drop started once the cavity occurred on the suction surface.

- (8) As the inlet pressure decreases, a symmetry cavitation corresponding to 2 or 3 times the rotational speed appeared. An asymmetry cavitation corresponding to the rotational speed also occurred. Cavitation surge occurred at low frequency when the inlet pressure decreases further. In cases of Z3s3 and Z3s2, rotating cavitation was strongly observed. On the other hand, rotating cavitation did not strongly occur in Z2s2. In Z3s2 case, it was found that the intensity of symmetry cavitation and rotating cavitation significantly weak compared with Z3s2. Especially, higher order rotating cavitation did not occur.

6.2 Recommendations for future work

It was proved that the effects of the blade number and the solidity on the hydraulic pressure rise, the work coefficient, and the efficiency. Moreover, the cavitation instabilities were also investigated. Future works will be needed as follow:

- (1) The new empirical equation did not exactly same compared with the experiment data. It seems that the new empirical equation did not

exactly same compared with the experiment data because the term was used that the efficiency is inversely proportional to the square root of the solidity. So the new efficiency empirical equation will be need the efforts to get the reliability for many other inducers.

- (2) The suction performance curve of only Z3s3 was slightly reduced to the pressure rise coefficient. The clear phenomenon investigation and the exact cause will be reviewed for the occurrence about some special inducers.
- (3) Cavitation instabilities using FFT analysis and visualization were examined. However, there was a limit to find phenomena and characteristics. So more detail methods such as the PIV will be required.

References

Acosta, A., 1958, "An Experimental Study of Cavitating Inducers," Proceedings of 2nd ONR Symposium, ONR/ACR-38, pp. 533-557. ASME, FEDSM2002-31201.

Ansys, Inc, 2006, "ANSYS CFX-solver Theory Guide," ANSYS CFX Release 11.0.

Ashihara, K., Goto, A., 2002, "Effects of Blade Loading on Pump Inducer Performance and Flow Fields," Proceedings of ASME, FEDSM2002-31201.

Ashihara, K., Goto, A., 2001, "Study on Turbopump Inducers Designed by 3-D Inverse Design Method," Proceedings of the AFI-2001.

Aungier, R., 2000, "Centrifugal Compressors: A Strategy for aerodynamic Design and Analysis."

Bakir, F., Kouidri, S., 1998, "Design and Analysis of Axial Inducer Performance," FEDSM98-5118.

Brennen, C.E., 1994, "Hydrodynamics of Pumps."

Brennen, C.E., 1995, "Cavitation and Bubble Dynamics."

Brennen, C.E., 2007, "The Amazing World of Bubbles."

Choi, C., Kim, J., 2009, "Effect of Number of Blades on the Performance of the Turbopump Inducer," Journal of KSFM, Vol. 12, pp. 52-57.

Cluff, R., Gorrell, S., 2013, "A Comparison of three-blades and four-bladed Inducers at On and Off Design Flow Rates," 49th AIAA/ASME/SAE/ASEE Joint Propulsion Conference.

David Japikse, 2001, "Overview of Industrial and Rocket Turbopump Inducer Design," 3th International Symposium on Cavitation

David Japikse, 1996, "Centrifugal Pump Design and Performance."

Dixon, S., 2010, "Fluid Mechanics and Thermodynamics of Turbomachinery," 6th edition.

Fujii, A, Azuma, S., 2002, "Unsteady Stress of 4-Bladed Inducer Blades and the Effect of Inlet Flow Distortion," JSME International Journal B, Vol. 45, No. 1, pp. 47-54.

Hong, S, Choi, C., 2004, "Effect of Solidity on the Performance of Turbopump Inducer," Transactions of the KSME B, Vol. 28, pp. 382-388.

Horiguchi, H., Watanabe, S., 2000, "A Theoretical Analysis of Alternate

Blade Cavitation in Inducers," Transactions of the ASME, Vol. 122, pp. 156-163.

Hwang, Y., 2013, "A Study on the Tip Leakage Flow Structures in an Azial Compressor with and without Slot Casing Treatment."

Kamijo, K., Yoshida M., 1993, "Hydraulic and Mechanical Performance of LE-7 LOX Pump Inducer," Journal of Propulsion and Power, Vol. 9, No. 6, pp. 819-826.

Kim, S., 2012, "Effect of Tip Clearance on Cavitation Performance and Flow Characteristics in a Turbopump Inducer."

Kimura, T., Yoshida Y., 2004, "Relation Between Geometries of Inducer and Backflow and Vortex Structures," 40thAIAA/ASME/SAE/ASEE Joint Propulsion Conference.

Lakshminarayana, B., 1982, "Fluid Dynamics of Inducers- a Review," Journal of Fluids Mechanics, Vol. 104, pp 411-427.

Lee, J., Kang, S., 2004, "Cavitation Test of a High Pressure Turbopump," Journal of KSFM, Vol. 7, pp. 16-23.

Lee, K., 2011, "Study on the Cavitation Performance and Its Instability of Two-Stage Inducer."

Lee, K., Kang, S., 2012, "Cavitation Performance and Instability of a Two-bladed Inducer," *Journal of Propulsion and Power*, Vol. 28, No. 6, pp. 1168-1175.

Lee, K., Kang, S., 2012, "Study on the Suppression of the Cavitation Instability in a Two-Stage Inducer," *Journal of Propulsion and Power*, Vol. 28, No. 5, pp. 946-954.

Lee, S., Jung, J., 1996, "Influence of Inducer Inlet Angle on Cavitation Flow and Suction Performance," *Transactions of the KSME B*, Vol. 20, pp. 1074-1082.

M. Shimagaki, M. Watanabe, 2006, "Effect of the Casing Configurations on the Internal Flow in Rocket Pump Inducer," 42nd AIAA/ASME/SAE/ASEE Joint Propulsion Conference.

Murayama, M., Tshjimoto, Y., 2006 "Unsteady Tip Leakage Vortex Cavitation Originating From the Tip Clearance of an Oscillating Hydrofoil," *Journal of Fluids Engineering*, Vol. 28, pp. 421-429.

O.Coutier, 2012, "Influence of Blade Number on Inducer Cavitating Behavior," *Journal of Fluids Engineering*, Vol. 134, No. 8.

Okita, K., Ugaajin, H., 2009, "Numerical Analysis of the Influence of the Tip Clearance Flows on the Unsteady Cavitating Flows in a

Three-Dimensional Inducer," *Journal of Hydrodynamics*, Vol. 21, pp. 34-40.

Pouffary, B., Patella, R., 2008, "Numerical Analysis of Cavitation Instabilities in Inducer Blade Cascade," *Journal of Fluids Engineering*, Vol. 130.

Rood, E., 1991, "Review-Mechanisms of Cavitation Inception," *Journal of Fluids Engineering*, Vol. 113, pp. 163-175.

Shimura, T., Shimagaki, Y., 2003, "Cavitation Induced Vibration of LE-7A Oxygen Turbopump," 5th International Symposium on Cavitation.

Tshjimoto, Y., Hironori H., 2005, "Backflow from Inducer and its Dynamics," ASME Fluid Division Summer Meeting and Exhibition, FEDSM2005-77381.

Tshjimoto, Y., Yoshiki Yoshida., 1997, "Observation of Oscillating Cavitation of an Inducer," *Journal of Fluids Engineering*, Vol. 119, pp 775-781.

Tshjimoto, Y., Yoshida Y., 2001, "Effect of Leading Edge Sweep on Unsteady Cavitation in Inducer(1st Report)," *Trans JSME*, Vol. 67, No. 662, pp. 32-36.

Tshjimoto, Y., 2006, "Cavitation Instabilities in Inducers," RTO-EN-AVT-143.

Tshjimoto, Y., Horiguchi, H., 2010, "Cavitation Instabilities in Turbopump Inducers - Analysis in 1-3 Dimensions-," International Journal of Fluid Machinery and Systems, Vol. 3, No. 2, pp. 170-180.

Watanabe, S., Sato, K., 1999, "Analysis of Rotating Cavitation in a Finite Pitch Cascade Using a Closed Cavity Model and a Singularity Method," Transactions of the ASME, Vol. 121, pp. 834-840.

Yedidiah, S., 1996, "Centrifugal Pump User's Guidebook," pp. 52-55.

Yoshida Y., Azuma, S., 2001, "Effect of Leading Edge Sweep on Unsteady Cavitation in Inducer(2nd Report)," Trans JSME, Vol. 67, No. 658, pp. 71-79.

터보펌프 인듀서의 날개 수와 현절비가 성능 및 캐비테이션 불안정성에 미치는 영향

서울대학교 대학원
기계항공공학부
강 병 윤

요 약

터보펌프 인듀서 설계에 있어서 여러 형상 변수를 선택하게 되는데 직경, 현절비 및 날개 각과 같은 변수들의 경우 기존에 많은 연구가 수행되었고, 합리적인 설계 개념과 범위를 제시하고 있다. 날개 수는 현절비와 관련이 있기는 하지만 단지 날개 수 변화에 대한 영향 평가는 미비하였다. 따라서 본 연구는 날개 수 변화에 대한 평가를 다루고 있다. 세 가지 형상의 인듀서를 대상으로 실험과 수치계산을 이용하여 분석하였다. 정확한 비교 검증을 위하여 측정 위치, 평균 방법, 그리고 변수 정의를 통일 하였고, 이에 대한 보정을 통하여 결과를 분석하였다. 압력 상승의 경우, 기본 인듀서가 가장 높았고, 현절비와 날개 수가 모두 증가한 인듀서, 그리고 동일한 현절비에 날개 수만 증가 한 인듀서 순서로 압력 상승이 감소하였다. 날개 뒷전에서는 경험식에서 제시한 대로 편차각이 분포하였지만, 출구를 지나오면서 인듀서의 직경이 줄어드는 효과로 인하여 편차각의 경향이 달라졌다. 그 결과로 접선방향 속도가 변하게 되었고, 이로 인해서 양정이 변하게 되었다. 효

율은 기본 인듀서가 가장 높은 점은 동일하였지만, 현절비와 날개 수가 모두 증가한 인듀서의 효율이 가장 낮았다. 상대 전압 손실과 혼합 손실이 가장 커서 효율이 변한 것으로 파악 되었다. 기존의 효율 경험식은 날개 수의 변화는 고려되어있지 않고, 현절비만 반영 된 함수였다. 따라서 날개 수 변화에 대한 영향을 고려하여 새로운 경험식을 제시하였다. 세 가지 형상으로는 표본이 부족하다고 판단하여 두 가지 형상을 추가하여 수치계산을 수행하였고, 이에 대한 결과를 반영하였다. 향 후 더욱 많은 형상에 대한 평가로 새로운 경험식에 대한 신뢰성을 확보해야 할 것이다. 실험과 수치계산을 통하여 캐비테이션 특성을 분석해 보았다. $NPSH_r$ (Required $NPSH$ or critical $NPSH$, 3% head drop point) 성능은 기존 형상 대비 25.8 % 와 14.1 % 증가하였다. 실험과 수치계산과의 결과는 큰 차이를 보였는데 수치 해석에 사용 된 캐비테이션 모델에서 원인을 찾을 수 있다. 캐비테이션 모델은 표면장력의 영향이 없다는 가정을 하였고, 증기의 발생과 억제에 관한 비선형의 수식을 계산의 편의를 위해서 선형화로 변경하였다. 따라서 수치 계산의 결과는 실제 이상 유동의 거동을 반영하지 못한 것으로 판단되었다. 캐비테이션 발생은 날개의 끝에서 팁 소용돌이 캐비테이션(Tip vortex cavitation)이 발생하고, 곧 이어 거품 캐비테이션(Bubble cavitation)이 나타난다. 캐비테이션 시작점(Inception)은 현절비의 변화와는 관련이 없고, 오직 날개 수 변화에만 영향을 받았다. 이는 시작점은 인듀서의 날개 끝에서 국소적으로 발생하는 현상이기 때문이다. 날개 수가 증가하면 유체와 날개와의 간섭이 증가하여 캐비테이션 시작이 빨리 발생한다. 캐비테이션이 시작하고 점차 진행이 되더라도 처음에는 양정의 감소가 없다. 입구 압력이 더욱 낮아지게 되면 양정이 감소하기 시작하는데, 이 지점에서의 유동특성을 살펴보면 다음과 같다. 인듀서 앞전(Leading edge)을 지나면 날개 길이(Chord)의 40 % 지점의 흡입면에서 압력 저하가 발생한다. 흡입면에서 발

생한 압력 저하는 다음 날개 길이의 20 % 지점의 압력면에도 영향을 미치게 된다. 증기압보다 낮은 압력에서 기포(Cavity)가 생성되면 양정이 감소하기 시작한다. 한 번 발생한 기포는 이 후 급격하게 커지게 되고 이로 인해 양정은 더욱 급격하게 하락하게 된다. 이 후 압력이 더욱 낮아지면 임계점(Critical point)을 지나 붕괴점(Breakdown)까지 이르게 된다. 날개 수가 3인 인듀서에서 나타나는 캐비테이션 불안정성의 가장 큰 특징은 회전 캐비테이션(Rotating cavitation)이다. 현절비 변화에 따른 캐비테이션 불안정성의 특징은 강도의 차이인데 비대칭 캐비테이션(Asymmetric cavitation)을 보면 확인 할 수 있다. 정확한 원인 규명과 현상 분석을 위해 PIV와 같은 정밀한 측정을 통한 분석이 필요하다고 생각된다.

주요어 : 터보펌프, 인듀서, 경협식, 캐비테이션, 유효흡입양정, 불안정성,
캐비테이션 시작점

학번 : 2008-22864